SYMMETRIC SINKHORN DIFFUSION OPERATORS

Anonymous authors

000

001 002 003

004

006

008 009

010

011

012

013

014

016

018

019

021

024

025 026

027 028 029

031

033

034

037

040

041

042

043

044 045

046

047

048

051 052 Paper under double-blind review

ABSTRACT

Smoothing a signal based on local neighborhoods is a core operation in machine learning and geometry processing. On well-structured domains such as vector spaces and manifolds, the Laplace operator derived from differential geometry offers a principled approach to smoothing via heat diffusion, with strong theoretical guarantees. However, constructing such Laplacians requires a carefully defined domain structure, which is not always available. Most practitioners thus rely on simple convolution kernels and message-passing layers, which are biased against the boundaries of the domain. We bridge this gap by introducing a broad class of smoothing operators, derived from general similarity or adjacency matrices, and demonstrate that they can be normalized into diffusion-like operators that inherit desirable properties from Laplacians. Our approach relies on a symmetric variant of the Sinkhorn algorithm, which rescales positive smoothing operators to match the structural behavior of heat diffusion. This construction enables Laplacian-like smoothing and processing of irregular data such as point clouds, sparse voxel grids or mixture of Gaussians. We show that the resulting operators not only approximate heat diffusion but also retain spectral information from the Laplacian itself, with applications to shape analysis and matching.

1 Introduction

Discrete Differential Geometry. Geometric data analysis is an active research field that provides a principled framework for understanding complex data (Gallot et al., 2004; Bronstein et al., 2021). These tools are especially effective in two or three dimensions, but also extend to graphs and higher-dimensional domains. While differential geometry provides elegant constructions on well-structured data, such as triangle meshes (Crane, 2018; Botsch et al., 2010), adapting these tools to less structured representations like point clouds or voxel grids remains a major challenge (Barill et al., 2018; Lachaud et al., 2023; Feng & Crane, 2024).

In many practical scenarios, high-quality triangular meshes are not available due to limitations in the acquisition process (Bogo et al., 2017) or even to the nature of the data itself (Behley et al., 2019). For example, in medical imaging, one often works with voxelized segmentation masks (Marcus et al., 2007) and anatomical structures such as trabecular bones that cannot be neatly described as surfaces. Similarly, point clouds and recent representations like Gaussian splats (Kerbl et al., 2023; Zhou & Lähner, 2025) are widely used, but typically lack explicit connectivity information. Using classical geometric operators in these settings often requires local approximations of the underlying manifold (Sharp & Crane, 2020; Sharp et al., 2022; Zhou & Lähner, 2025), which can introduce significant errors and degrade performance.

Smoothing Operations. Bridging the gap between geometry-aware methods designed for clean meshes and more general unstructured data representations is crucial for scalable learning with shapes. Among the most fundamental operations in geometry processing is *smoothing*, which modifies a signal using local geometric information (Taubin, 1995; Sharp et al., 2022). A key example is *heat diffusion*, which, on meshes, is controlled by the matrix exponential of the Laplacian (Gallot et al., 2004). This process plays a central role in many pipelines for shape analysis (Crane et al., 2017), segmentation (Sharp et al., 2022), and correspondence (Sun et al., 2009).

Contributions. In this work, we generalize heat diffusion to arbitrary discrete domains such as point clouds, voxel grids, Gaussian mixtures and binary masks. Our approach ensures *mass con-*

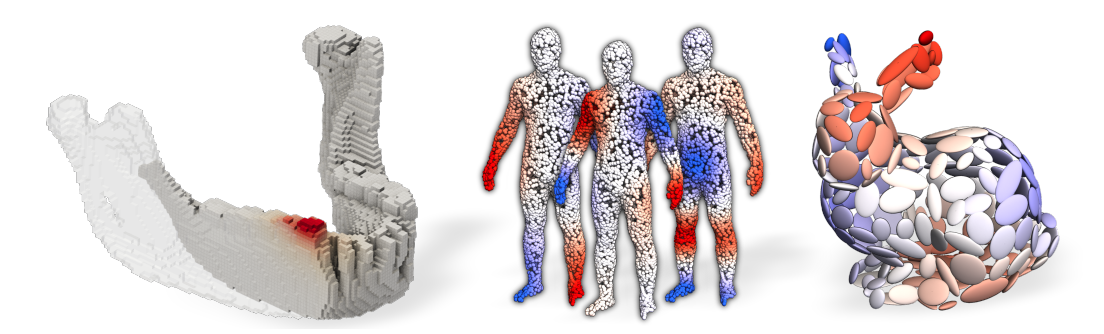


Figure 1: Heat-like diffusion and spectral analysis on general geometric data without Laplacian inversion. **Left:** Mass-preserving diffusion of a Dirac function on a sparse voxel grid (jaw bone). **Right:** Laplacian-like eigenvectors on a point cloud (human) and Gaussian mixture (bunny).

servation, meaning that the total sum of the signal remains constant under diffusion, corresponding to physical conservation of heat over the domain. Our approach starts from a symmetric similarity matrix, akin to an adjacency matrix, and produces a heat-diffusion-like operator via a symmetric Sinkhorn normalization (Knight et al., 2014). This results in a linear operator, symmetric with respect to a mass-weighted inner product, whose properties and spectrum closely resemble that of the exponential of a Laplacian, as displayed on Figure 1. Our contributions can be summarized as follows:

- We present an algebraic framework for defining smoothing, Laplacians and diffusions on general discrete geometric representations, clarifying their shared structure and assumptions.
- We propose an efficient and GPU-friendly algorithm to transform symmetric similarity matrices into mass-preserving diffusion operators, inspired by recent theoretical works in manifold learning (Wormell & Reich, 2021; Cheng & Landa, 2024) and optimal transport (Feydy et al., 2019).
- We demonstrate broad applicability to geometric data analysis, particularly for statistical shape analysis and generative modelling.

2 RELATED WORKS

Laplacians and Heat Diffusions. The Laplace–Beltrami operator Δ is an essential tool in discrete geometry processing, especially on triangle meshes (Sorkine, 2005; Botsch et al., 2010). Its spectral properties have been widely used for shape analysis (Reuter et al., 2006) and correspondence (Levy, 2006; Ovsjanikov et al., 2012). A closely related tool is the heat equation $\partial_t f = -\Delta f$, whose solution $f(t) = e^{-t\Delta} f_0$ acts as a smoothing operator on an initial signal f_0 . Heat diffusion has been leveraged to compute shape descriptors (Sun et al., 2009; Bronstein & Kokkinos, 2010), geodesic distances (Crane et al., 2017; Feng & Crane, 2024) parallel transport (Sharp et al., 2019b) or shape correspondences (Vestner et al., 2017; Cao et al., 2025). Heat-based smoothing has also inspired neural architectures for geometric learning (Sharp et al., 2022; Gao et al., 2024) and generative modelling (Yang et al., 2023). Crucially, the matrix exponential $e^{-t\Delta}$ is rarely computed directly. Instead, practical implementations rely on either implicit Euler integration (Botsch et al., 2010) or spectral truncation using the first Laplacian eigenfunctions (Sharp et al., 2022). These approaches rely on mesh-based discretizations of the Laplacian (Pinkall & Polthier, 1993; Meyer et al., 2003; Sharp et al., 2019a) and pre-computed factorizations, such as Cholesky or sparse eigendecompositions, limiting scalability and flexibility. While extensions to non-manifold triangulations have been proposed (Sharp & Crane, 2020; Belkin et al., 2009), generalizing diffusion-based smoothing to higher-dimensional or unstructured data such as noisy point clouds and sparse voxel grids remains challenging.

Graph Laplacians. The Laplacian also plays a central role in graph-based learning and analysis (Chung, 1997), supporting spectral clustering (von Luxburg, 2007), embedding, and diffusion.

Unlike the cotangent Laplacian for mesh processing (Pinkall & Polthier, 1993; Meyer et al., 2003), the graph Laplacian relies only on connectivity and optional edge weights, making it applicable to a broader range of data. Discrete approximations of heat diffusion, such as the explicit Euler step $I-t\Delta$, form the basis of many graph neural networks (GNNs) (Kipf & Welling, 2017; Hamilton et al., 2017; Chamberlain et al., 2021). Recent works explore approximations of implicit time-stepping schemes (Behmanesh et al., 2023; Chamberlain et al., 2021) but lose key properties or limit the flexibility of the diffusion. Beyond Laplacians, message passing (Gilmer et al., 2017) or graph attention (Veličković et al., 2018) offer alternative forms of smoothing. In this work, we take a step back and propose *general axioms* for defining smoothing operators on discrete domains, formalizing desirable properties such as symmetry or mass conservation. We show that popular approaches, as well as various Laplacian normalization techniques (e.g., symmetric, random-walk) can be interpreted as specific cases in this framework. These classical methods often trade-off symmetry or mass preservation. To address this, we study a *Sinkhorn normalization* that satisfies these properties jointly, producing operators which are symmetric under a mass-weighted inner product and spectrally similar to Laplacian exponentials, while remaining compatible with unstructured geometric data.

Sinkhorn Scaling. The Sinkhorn algorithm (Sinkhorn & Knopp, 1967) scales a nonnegative matrix into a doubly stochastic one via alternating row and column normalizations, and is widely used in machine learning (Cuturi, 2013) thanks to its efficiency and GPU compatibility. For symmetric inputs, a symmetry-preserving variant yields symmetric and doubly stochastic operators (Knight et al., 2014). Recent work applies Sinkhorn normalization to graph Laplacians for manifold learning and dimension reduction, with theoretical guarantees (Marshall & Coifman, 2019; Wormell & Reich, 2021; Cheng & Landa, 2024). We extend this idea to a geometry-aware setting by introducing a domain-specific mass matrix that induces a weighted inner product. Rather than enforcing bistochasticity, we construct operators that are row-stochastic and symmetric with respect to this inner product. The resulting kernel Q satisfies $(MQ)^{\top} = MQ$, where M encodes local geometric mass (for example, triangle areas or voxel densities). This ensures exact mass conservation and symmetry under the induced inner product, aligning the discrete diffusion with its continuous analogue. To our knowledge, such mass-preserving normalization has not been used to define smoothing operators on general discrete geometric structures.

Generalization to Unstructured Data. Extending differential operators to unstructured data remains an open challenge. While regular grids support Laplacian-based smoothing or convolutional approaches, more irregular representations, such as point clouds or gaussian splats, typically rely on local approximations or learned kernels (Wu et al., 2019; Sharp & Crane, 2020; Sharp et al., 2022; Zhou & Lähner, 2025). Our framework requires only a notion of similarity between points, and provides a unified approach to smoothing across these modalities. This allows us to bridge the gap between discrete differential operators and modern unstructured data representations, without relying on consistent manifold assumptions or expensive linear algebra routines.

3 WARM-UP: GRAPHS

To build intuition about our framework, we begin with a simple example on an undirected graph \mathcal{G} with vertex set \mathcal{V} and edge set \mathcal{E} (see Figure 2). In this section, we illustrate two approaches to smoothing a signal $f \in \mathbb{R}^{\mathcal{V}}$ defined on the graph vertices.

Laplacian Smoothing. A common method to quantify the regularity of f is to use a discrete derivative operator $\delta \in \{0,\pm 1\}^{\mathcal{E} \times \mathcal{V}}$, which encodes differences across edges. This induces a Dirichlet energy $E(f) = \frac{1}{2} \|\delta f\|^2 = \frac{1}{2} (\delta f)^\top \delta f$, that can be rewritten as $E(f) = \frac{1}{2} f^\top \Delta f$, where $\Delta = \delta^\top \delta$ is a symmetric positive semi-definite matrix acting as a discrete Laplacian. The matrix Δ admits an orthonormal eigendecomposition with eigenvectors (Φ_i) and non-negative eigenvalues (λ_i^Δ) . Low values of $E(\Phi_i) = \lambda_i^\Delta/2$ correspond to smoother eigenfunctions. The eigenvectors can thus be interpreted as frequency modes: $\lambda_1^\Delta = 0$ corresponds to the constant function, while higher eigenvalues λ_i^Δ capture finer variations.

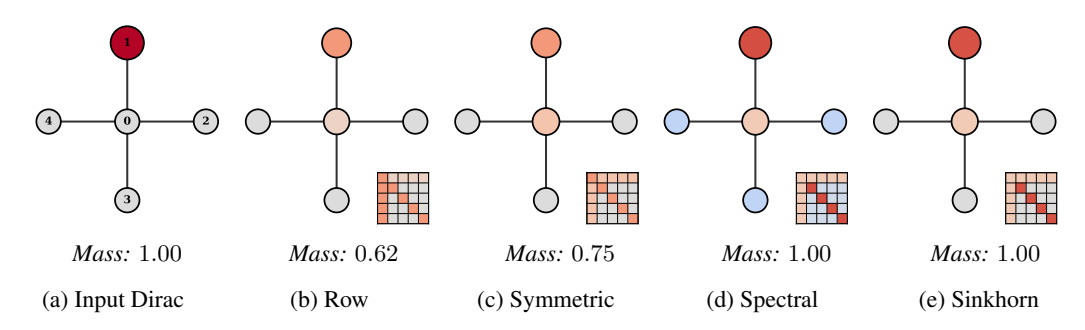


Figure 2: Diffusion of a Dirac function for different normalizations of the raw smoothing operator K. Row and symmetric normalizations distort mass, while a truncated spectral approximation that uses 4 out of 5 eigenvectors introduces negative values (in blue). In contrast, our symmetric Sinkhorn normalization preserves both positivity and mass. The full diffusion matrices are shown as insets

Heat diffusion, governed by the operator $e^{-t\Delta}$, acts as a smoothing transform that damps high-frequency components while preserving the low-frequencies. If $f = \sum_i \widehat{f}_i \Phi_i$, then:

$$E(e^{-t\Delta}f) = \frac{1}{2} \sum_{i} \lambda_{i}^{\Delta} e^{-2t\lambda_{i}^{\Delta}} \hat{f}_{i}^{2} \leq \frac{1}{2} \sum_{i} \lambda_{i}^{\Delta} \hat{f}_{i}^{2} = E(f).$$
 (1)

By construction, diffusion regularizes input functions and converges as $t \to \infty$ to a constant signal \widehat{f}_1 . Remarkably, the *total mass* of the signal is also preserved for all t: if $\langle \cdot, \cdot \rangle$ denotes the dot product and 1 is the constant vector, then $\langle 1, e^{-t\Delta} f \rangle = \langle 1, f \rangle$. This follows from the symmetry of $e^{-t\Delta}$ and the fact that constant functions are fixed points of the heat flow: $e^{-t\Delta}1 = 1$. Lastly, all entries of $e^{-t\Delta}$ are non-negative, ensuring that non-negative input signals remain non-negative. This follows from $-\Delta$ being a Metzler matrix (Berman & Plemmons, 1994) (with non-negative off-diagonal entries), which guarantees entrywise positivity of the matrix exponential.

While the Laplacian exponential provides strong regularization properties, its computation is expensive in practice. Most authors rely on the implicit Euler scheme $(I+t\Delta)^{-1}f$ which guarantees numerical stability but requires solving a linear system for every new signal f.

Message-passing and Local Averages. A common alternative is to apply local averaging operators derived from the graph's adjacency matrix A. One simple choice is to use the linear operator $K = \frac{1}{2}(D+A)$, where $D = \operatorname{diag}(A1)$ is the diagonal degree matrix. However, this raw smoothing operator K lacks key properties of $e^{-t\Delta}$ and is highly sensitive to vertex degrees: well-connected vertices disproportionately influence the output, while low-degree nodes contribute less. This introduces a bias at boundaries of the domain that is undesirable in many applications.

Several methods have been proposed to mitigate this issue (Chung, 1997; Coifman & Lafon, 2006):

- 1. Row normalization divides each row of K by the degree of the corresponding vertex. This yields the operator $D^{-1}K$ that performs a local averaging but breaks symmetry.
- 2. **Symmetric normalization** restores symmetry via $D^{-\frac{1}{2}}KD^{-\frac{1}{2}}$, but does not preserve constant input signals.
- 3. **Spectral methods** approximate the heat diffusion operator $e^{-t\Delta}$ as a low-rank matrix $\sum_{i=1}^{R} e^{-t\lambda_i^{\Delta}} \Phi_i \Phi_i^{\top}$ in the span of the first R eigenvectors of the Laplacian Δ . While this preserves desirable diffusion properties, computing these eigenvectors is expensive and truncation introduces undesirable ringing artifacts.

Bi-Stochastic Normalization. As illustrated in Figures 2b to 2d, existing normalization strategies fail to fully capture the desired properties of heat diffusion. The *Sinkhorn* or *bi-stochastic* scaling method has recently emerged as a principled alternative, combining the benefits of both row-wise and symmetric normalization while avoiding the numerical pitfalls of spectral methods. The core idea is to apply symmetric normalization iteratively until convergence. Under mild assumptions, there exists a unique positive diagonal matrix Λ such that the rescaled operator $\Lambda K\Lambda$ is both symmetric and mass-preserving, as illustrated in Figure 2e. Strong convergence results have already

been obtained in the context of point clouds sampled uniformly on a compact manifold (Wormell & Reich, 2021; Cheng & Landa, 2024). As part of our framework, we extend the Sinkhorn method to support additional data structures (voxel grids, Gaussian mixtures), with theoretical guarantees and practical applications to geometric data analysis.

4 THEORETICAL ANALYSIS

Notations. We now introduce our framework in full generality. Let $\mathcal{X} \subset \mathbb{R}^d$ be a bounded domain, endowed with a positive Radon measure μ . We consider signals $f: \mathcal{X} \to \mathbb{R}$ in the space $L^2_{\mu}(\mathcal{X})$ of square-integrable functions, endowed with the inner product $\langle f, g \rangle_{\mu} = \int_{\mathcal{X}} f(x)g(x) \, \mathrm{d}\mu(x)$. We define the *mass* of a function as $\langle f, 1 \rangle_{\mu} = \int_{X} f(x) \, \mathrm{d}\mu(x)$. When the measure $\mu = \sum_{i=1}^{N} m_i \delta_{x_i}$ is discrete, functions f can be identified with column vectors $(f(x_1), \ldots, f(x_N))$ and μ corresponds to a positive diagonal matrix $M = \mathrm{diag}(m_1, \ldots, m_N) \in \mathbb{R}^{N \times N}$. The inner product becomes $\langle f, g \rangle_{\mu} = f^{\top} Mg$: we use $\langle \cdot, \cdot \rangle_{\mu}$ or $\langle \cdot, \cdot \rangle_{M}$ interchangeably depending on context.

We denote by $A^{\top_{\mu}}$ (or $A^{\top_{M}}$), the adjoint of a linear operator $A:L^{2}_{\mu}(\mathcal{X})\to L^{2}_{\mu}(\mathcal{X})$ with respect to the μ -weighted inner product. In the finite case, this corresponds to $A^{\top_{M}}=M^{-1}A^{\top}M$ so that:

$$\langle f, Ag \rangle_M = f^{\mathsf{T}} M Ag = g^{\mathsf{T}} M M^{-1} A^{\mathsf{T}} M f = \langle g, A^{\mathsf{T}_M} f \rangle_M, \tag{2}$$

where A^{\top} is the standard transpose. A matrix is symmetric with respect to the weighted dot product $\langle \cdot, \cdot \rangle_M$ if and only if it is of the form S = KM with $K^{\top} = K$.

Laplace-like Operators. As introduced in Section 3, Laplacians capture local variations of functions on a domain. We highlight the key structural properties of such operators, simplifying the list that was identified by Wardetzky et al. (2008) for surface triangle meshes:

Definition 4.1 (Laplace-like Operators). A Laplace-like operator is a linear map $\Delta: L^2_{\mu}(\mathcal{X}) \to L^2_{\mu}(\mathcal{X})$, identified with a matrix (Δ_{ij}) in the discrete case, that satisfies the following properties:

- $\begin{array}{ll} (i) & \textit{Symmetry: } \Delta^{\top_{\mu}} = \Delta \\ (ii) & \textit{Constant cancellation: } \Delta 1 = 0 \end{array} \qquad \begin{array}{ll} (iii) & \textit{Positivity: } \langle f, \Delta f \rangle_{\mu} \geq 0 \textit{ for all } f \in L^2_{\mu}(\mathcal{X}) \\ (iv) & \textit{Off-Diagonal Negativity: } \Delta_{ij} \leq 0 \textit{ for } i \neq j \end{array}$
- Properties (i), (ii) and (iii) reflect the classical construction of Laplacians as self-adjoint positive semi-definite operators, typically derived from integration by parts: $\langle \nabla f, \nabla g \rangle_{\mu} = \langle f, \Delta g \rangle_{\mu}$. Condition (iv) which corresponds to a Metzler structure (Berman & Plemmons, 1994) in the discrete

dition (iv), which corresponds to a *Metzler* structure (Berman & Plemmons, 1994) in the discrete setting, ensures intuitive diffusion behavior: diffusing a signal with $\partial_t f = -\Delta f$ causes mass to flow outwards (Wardetzky et al., 2008). We refer to Appendix A for a definition in the continuous case using Kato's inequality (Arendt, 1984).

These conditions are easily verified for the standard graph Laplacian. On triangle meshes, the commonly used cotangent Laplacian satisfies properties (i)–(iii) by construction. However, property (iv) only holds in the absence of obtuse angles. Violations of this condition, which results in undesirable positive weights, are a well-known issue in geometry processing, typically addressed using intrinsic triangulations (Bobenko & Springborn, 2007; Fisher et al., 2006; Sharp et al., 2019a).

Diffusion Operators. As presented in Section 3, the family of diffusion operators $e^{-t\Delta}$ associated to a Laplacian Δ play a central role in geometry processing and learning. These operators smooth input signals while preserving key structural properties. Leveraging the properties of Definition 4.1 we define diffusion operators as follows:

Definition 4.2 (Diffusion Operators). A diffusion operator is a linear map $Q: L^2_{\mu}(\mathcal{X}) \to L^2_{\mu}(\mathcal{X})$ that satisfies the following properties:

- (i) Symmetry: $Q^{\top_{\mu}} = Q$ (iii) Damping: The eigenvalues of Q lie in [0, 1] (iv) Entrywise positivity: Qf > 0 whenever f > 0
- Laplace-like operators and diffusion operators are almost equivalent: the exponential of an any Laplace-like operator yields a diffusion operator, while the principal logarithm of a diffusion operator yields properties (i)-(iii) of Definition 4.1. Property (iv) in Definition 4.2 is slightly weaker: true equivalence would require Q^t to be entrywise positive for all $t \geq 0$; see Appendix A.

Algorithm 1 Symmetric Sinkhorn Normalization

Require: Smoothing matrix $S \in \mathbb{R}^{N \times N}$ $\triangleright S = KM$ where $K^{\top} = K$ and M is a mass matrix.1: Initialize $\Lambda \leftarrow I_N$ $\triangleright \Lambda$ is a diagonal matrix, stored as a vector of size N.2: while $\sum_i |\Lambda_{ii} \sum_j S_{ij} \Lambda_{jj} - 1|$ is larger than a tolerance parameter \mathbf{do} 3: $d_i \leftarrow \sum_j S_{ij} \Lambda_{jj}$ \triangleright Matrix-vector product with S.4: $\Lambda_{ii} \leftarrow \sqrt{\Lambda_{ii}/d_i}$ \triangleright Coordinate-wise update on a vector of size N.5: end while \triangleright The diffusion Q is a positive scaling of S.

These properties reflect the structure of classical heat diffusion. Symmetry and constant preservation imply mass conservation, since for any f, $\langle 1,Qf\rangle_{\mu}=\langle Q^{\top_{\mu}}1,f\rangle_{\mu}=\langle Q1,f\rangle_{\mu}=\langle 1,f\rangle_{\mu}$. Entrywise positivity (iv) follows from the non-negativity of the heat kernel: a discrete perspective via Metzler matrices is given in Appendix A. Damping (iii) ensures that repeated applications of Q attenuate high-frequency components.

Finally, when $Q=e^{-t\Delta}$, its leading eigenvectors coincide with the lowest-frequency modes of Δ , with $\lambda_i^Q=e^{-t\lambda_i^\Delta}$. This allows one to recover low-frequency Laplacian structure via power iterations on Q, without computing small eigenpairs directly (see Section 6).

Smoothing Operators. In practice, defining a diffusion operator without access to an underlying Laplacian can be challenging. Instead, many operators commonly used in geometry processing, such as adjacency or similarity matrices, implicitly encode local neighborhood structures and enable function smoothing through local averaging. We refer to such matrices as *smoothing operators*:

Definition 4.3 (Smoothing Operators). A smoothing operator is a linear map $S: L^2_{\mu}(\mathcal{X}) \to L^2_{\mu}(\mathcal{X})$, identified with a matrix (S_{ij}) in the discrete case, that satisfies the following properties:

- (i) Symmetry: $S^{\top_{\mu}} = S$, so S = KM with $K^{\top} = K$ in the discrete case
- (ii) Operator positivity: $\langle f, Sf \rangle_{\mu} \geq 0$ for all f, so the eigenvalues of S lie in $[0, +\infty)$
- (iii) Entrywise positivity: $Sf \ge 0$ whenever $f \ge 0$, so $S_{ij} \ge 0$ in the discrete case

Sinkhorn Normalization. As discussed in Section 3, recent works in manifold learning have shown that symmetric graph adjacency matrices can be rescaled to become bi-stochastic at minimal computational cost. We leverage this insight to derive the following two results:

Theorem 4.1 (Symmetric Normalization). Let $\mu = \sum_{i=1}^{N} m_i \delta_{x_i}$ be a finite discrete measure with positive weights $m_i > 0$, and S a smoothing operator encoded as a N-by-N matrix with positive coefficients $S_{ij} > 0$. Then, Algorithm 1 converges to the unique diagonal matrix Λ with positive coefficients such that $Q = \Lambda S \Lambda$ is a diffusion operator with respect to μ .

Theorem 4.2 (Convergence for the Gaussian and Exponential Kernels). Let \mathcal{X} be a bounded region of \mathbb{R}^d , and $(\mu^t)_{t\in\mathbb{N}}$ be a sequence of finite discrete measures $\mu^t = \sum_{i=1}^{N_t} m_i^t \delta_{x_i^t}$ that converges weakly to a (possibly continuous) Radon measure μ with positive, finite total mass.

Let k(x,y) be a Gaussian or exponential kernel with positive radius $\sigma > 0$, and define the smoothing operators $S_{ij}^t = k(x_i^t, x_j^t) m_j^t$. Let $Q^t = \Lambda^t S^t \Lambda^t$ be the diffusion operators obtained via symmetric normalization as in Theorem 4.1.

Then, each diagonal matrix Λ^t can be interpeted as a pointwise product $(f \mapsto \lambda^t f)$ with a continuous positive function $\lambda^t : \mathcal{X} \to \mathbb{R}_+$ such that $\Lambda^t = \operatorname{diag}(\lambda^t(x_1^t), \dots, \lambda^t(x_{N_t}^t))$. Also, there exists a continuous positive function $\lambda : x \in \mathcal{X} \mapsto \lambda(x) > 0$ such that:

$$Q: f \in L^2_{\mu}(\mathcal{X}) \mapsto \left[Qf: x \mapsto \lambda(x) \int_{\mathcal{X}} k(x, y) \lambda(y) f(y) \, \mathrm{d}\mu(y) \right] \in L^2_{\mu}(\mathcal{X}) \tag{3}$$

is a diffusion operator, and Q^t converges pointwise to Q. For all continuous signal f on \mathcal{X} ,

$$\left[Q^t f: x \mapsto \lambda^t(x) \sum_{j=1}^{N_t} k(x, x_j^t) m_j^t \lambda^t(x_j^t) f(x_j^t) \right] \xrightarrow{t \to +\infty} Qf \text{ uniformly on } \mathcal{X}. \tag{4}$$

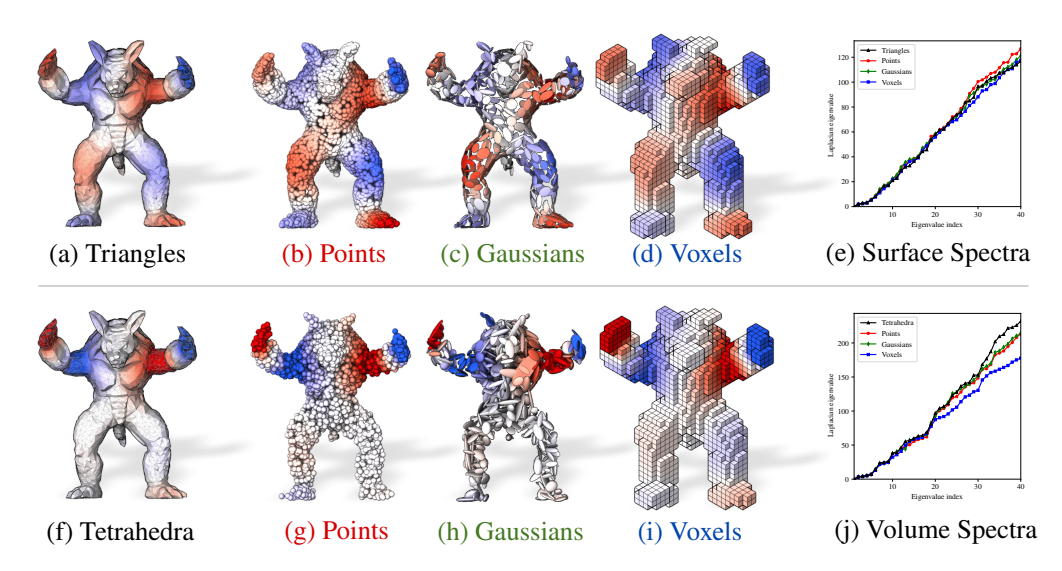


Figure 3: Spectral analysis on the Stanford Armadillo (Krishnamurthy & Levoy, 1996) normalized to the unit sphere, treated as a surface (top) and volume (bottom). We compare the reference cotan Laplacian (a,f) to our normalized diffusion operators on clouds of 5 000 points (b,g), mixtures of 500 Gaussians (c,h) and binary voxel masks (d,i), all using a Gaussian kernel of radius $\sigma = 0.05$ (edge length of a voxel). We display the 10th eigenvector (a–d,f–i) and the first 40 eigenvalues (e,j).

This result provides a practical convergence guarantee for our construction: under fixed kernel scale $\sigma>0$ and increasing sample resolution, the normalized operators Q^t converge to a continuous diffusion operator Q (proofs in Appendices B and C). In contrast, the manifold-learning literature finds Laplace-Beltrami consistency in joint limit $N\to\infty,\ \sigma\to0$ (with density corrections) for Sinkhorn normalizations (Wormell & Reich, 2021; Cheng & Landa, 2024). Our results *complement* that line and target the fixed-scale regime used in practice and provide a simple normalization that makes each Q^t symmetric, mass-preserving, entrywise positive, and spectrally confined to [0,1]. Note that we assume finite samples and positive entries in S, and refer to Knight et al. (2014, Sec. 3.1) for zero entries.

5 EFFICIENT IMPLEMENTATION

Sinkhorn Convergence and Versatility. We use the symmetric Sinkhorn algorithm (Knight et al., 2014; Feydy et al., 2019), which converges in a few iterations, as shown in Appendix D. Following scipy.sparse.linalg (Virtanen et al., 2020), we treat S as a black-box matrix-vector product: no factorization or complex data structure is required as diffusion behavior is encoded entirely in the diagonal Λ . Code will be released upon acceptance.

Graphs. Given a symmetric adjacency matrix $A \ge 0$, regularize $A_\varepsilon = A + \varepsilon 11^\top$ ($\varepsilon > 0$). With vertex masses $M = \operatorname{diag}(m_i)$ and degree matrix D, set $S = (D + A_\varepsilon)M$, which satisfies Definition 4.3 and is efficient when A is sparse. Weak diagonal dominance (Horn & Johnson, 1985) ensures a positive spectrum.

Point Clouds and Gaussian Mixtures. Given a weighted point cloud (x_i, m_i) , we use Gaussian kernels k with $S_{ij} = k(x_i, x_j)m_j$ for smoothing. Matrix-vector products scale to millions of points via the KeOps library (Charlier et al., 2021; Feydy et al., 2020) or optimized attention layers (Lefaudeux et al., 2022; Dao, 2023) (described in Appendix D).

For Gaussian Mixtures, given a pair $m_i \mathcal{N}(x_i, \Sigma_i)$ and $m_j \mathcal{N}(x_j, \Sigma_j)$, we use the L^2 dot product of densities convolved with an isotropic Gaussian of variance $\sigma^2/2$:

$$S_{ij} = m_j \exp\left[-\frac{1}{2}(x_i - x_j)^{\top} (\sigma^2 I + \Sigma_i + \Sigma_j)^{-1} (x_i - x_j)\right].$$
 (5)

Multiplicative constants are normalized out by Algorithm 1.

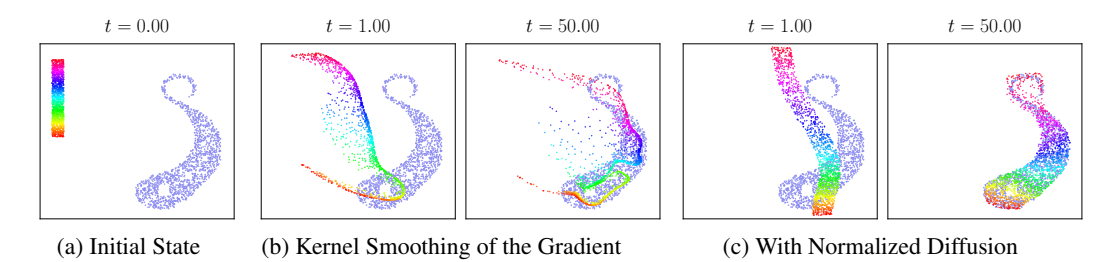


Figure 4: Flow of a source distribution of points (rainbow) towards a target (blue), following the gradient of the Energy Distance for a Gaussian kernel metric (b) and its normalized counterpart (c).

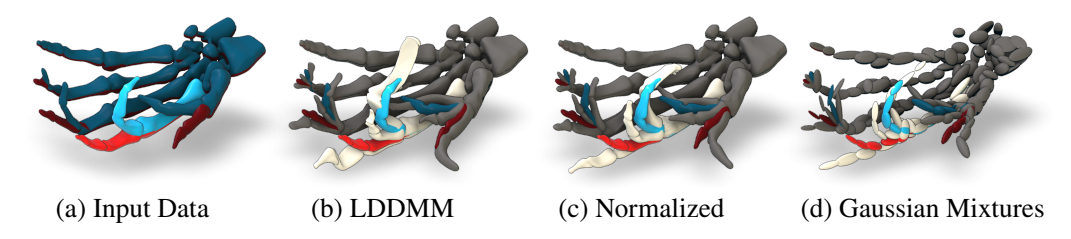


Figure 5: Pose interpolation and extrapolation of a human hand skeleton. (a) We interpolate between source (t=0, red) and target (t=1, blue) poses, and extrapolate to $t=-0.5,\,0.5,\,$ and 1.5. (b) The standard LDDMM geodesic with a Gaussian kernel ($\sigma=0.1$) produces unrealistic extrapolations. (c) Using our normalized diffusion yields a smoother, more plausible path. (d) The method remains robust on coarse Gaussian-mixture inputs (100 components).

Voxel Grids. On regular grids, Gaussian smoothing is implemented as a *separable* convolution. For sparse volumes, we leverage the efficient data structures of the Taichi library (Hu et al., 2019).

6 RESULTS

Spectral Shape Analysis. As discussed in Section 4, we expect the leading eigenvectors of a diffusion operator Q to approximate low-frequency Laplacian modes. Figure 3 compares our operators across modalities to a FEM Laplacian on meshes, and showcase additional results on the sphere and cube in Appendix F. We also provide simple heuristics to estimate Laplacian eigenvalues from our normalized diffusion operators (see App. F) and show in Figure 3 (Right) that their distributions remain consistent across modalities, with deviations emerging near the voxel sampling scale.

Normalized Metrics. Laplacians naturally induce Sobolev metrics and simple elastic penalties, commonly used as regularizers in machine learning and applied mathematics.

Figure 4 show results following Feydy et al. (2019) by minimizing the Energy Distance (Rizzo & Székely, 2016) between two point clouds, but smoothing the gradient with a Gaussian kernel. Replacing raw Gaussian smoothing with our normalized diffusion improves stability near boundaries and accelerates convergence in the Energy–Distance flow. This suggests potential in inverse rendering (Nicolet et al., 2021) or generative modelling (Liu & Wang, 2016; Arbel et al., 2019; Korba et al., 2024). We detail the objective, discretization, and parameters in Appendix G.

In Figure 5, we follow Kilian et al. (2007) and perform a geodesic interpolation between two poses of an anatomical shape. Standard metrics for surface meshes such as ARAP (Sorkine & Alexa, 2007) or elastic shell models (Grinspun et al., 2003; Sassen et al., 2024) work well on clean meshes, but are not robust to topological noise. Computational anatomy instead uses spline and kernel metrics (Bookstein, 1989; Pennec et al., 2019), defining a diffeomorphic shape space via LDDMM (Beg et al., 2005; Durrleman et al., 2014). For very large deformations, however, kernel metrics tend to favor contraction–expansion rather than pure translations (Micheli et al., 2012) (see Figure 5b). Replacing the raw kernel K by our normalized diffusion Q within LDDMM mitigates this and yields

Table 1: **Left:** Shape correspondence accuracy of Q-DiffNet on FAUST, SCAPE, and SHREC19 (*lower is better*). **Right:** Wall-clock runtimes for symmetric Sinkhorn normalization (5 iterations) on the GPU, compared to CPU runtimes for implicit Laplacian diffusion using sparse LU.

(a) Runtime (ms) vs. N

(b) Mean Geodesic Error

N	GPU Sinkhorn	CPU LU
10 000	3	65
50000	21	393
100000	89	1030
250000	448	3510
500000	1817	9100
1000000	6789	23600

Method	FAUST	SCAPE	S19
DiffNet	1.6	2.2	4.5
ULRSSM	1.6	2.1	4.6
DiffNet (PC)	3.0	2.5	7.5
ULRSSM (PC)	2.3	2.4	5.1
Q-DiffNet (QFM)	2.5	3.1	4.1
Q-DiffNet	2.1	2.4	3.5

more plausible paths across arbitrary data structures (Figure 5c–d). Full equations and implementation details are provided in Appendix G.

Runtimes. Our symmetric Sinkhorn converges in 5–10 iterations across modalities (see curves in Appendix D). We report *GPU runtimes* for 5 iterations using a Gaussian kernel for point clouds of increasing size. These are compared to *CPU runtimes* for implicit Laplacian diffusion using sparse LU factorization, which reflects typical usage *when a Laplacian is available*. Dense solvers on the GPU are significantly slower and run out of memory beyond 10k points. Additional details on hardware, experimental setup, and other baselines are provided in Appendix E.

Point Feature Learning. We evaluate our operator on 3D shape correspondence, where the goal is to match points across human shapes in varying poses, a challenging task due to changes in geometry and topology. Building on DiffusionNet (Sharp et al., 2022), we replace its spectral smoothing with our kernel-based operator, resulting in Q-DiffNet, which operates directly on 3D coordinates and learns diffusion scales (σ_i) instead of fixed times. We integrate Q-DiffNet into the ULRSSM pipeline (Cao et al., 2023), train on the remeshed FAUST+SCAPE datasets (Bogo et al., 2014; Anguelov et al., 2005; Ren et al., 2019) using point clouds, and also evaluate on the harder SHREC19 benchmark (Melzi et al., 2019). We compare to reference mesh-based methods (Sharp et al., 2022; Cao et al., 2023), and to their point-cloud retrainings ("PC"). As shown in Table 1b, Q-DiffNet outperforms point-based baselines on SHREC19 and remains competitive with all methods on FAUST and SCAPE. While our network avoids Laplacian eigenvectors, ULRSSM still uses them for functional maps and we also report a variant using eigenvectors from our operator ("QFM"). The operator thus acts as a geometry-aware module applicable to broader shape representations, including partial data (Attaiki et al., 2021). Implementation details and qualitative results are in Appendix I.

7 CONCLUSION AND FUTURE WORKS

We introduced a theoretical and practical framework for defining heat-like diffusion operators on general geometric data. Our approach unifies and extends classical constructions such as graph adjacency or similarity matrices into well-behaved diffusion mechanisms. We demonstrated its versatility across tasks, including Laplacian eigenvector approximation, gradient flow stabilization, and integration into neural networks as stable geometry-aware layers.

While our experiments confirm the promise of this framework, they remain preliminary. Future work should explore more extensive downstream applications, particularly in settings where standard Laplacians are unavailable or unreliable. In addition, the scalability of our method can be further improved: while our current implementation benefits from GPU-accelerated libraries, incorporating ideas from sparse or low-rank attention mechanisms could yield significant runtime gains on large-scale point clouds and volumetric data.

REPRODUCTIBILITY STATEMENT

Our main algorithm is summarized in Algorithm 1. Regarding our theoretical contributions, we state all axioms and definitions in Section 4 with more details in Appendix A, and provide complete proofs of the two main theorems in Appendices B and C. Implementation details needed to reproduce all results are given for each experiment: convergence behavior and practical notes in Appendix D, runtime setup and hardware in Appendix E, eigenvector estimation and heuristics in Appendix F, gradient-flow objectives and discretization in Appendix G, LDDMM geodesic shooting in Appendix H, and training protocol for Q-DiffNet Appendix I. We also include a timings table in Table 1a and report iteration counts so others can budget runs. Together, these materials are sufficient to reproduce the figures and tables from scratch.

Complete code for full reproducibility will be made public upon acceptance.

REFERENCES

- Dragomir Anguelov, Praveen Srinivasan, Daphne Koller, Sebastian Thrun, Jim Rodgers, and James Davis. SCAPE: Shape completion and animation of people. *ACM Transactions on Graphics*, 24 (3):408–416, July 2005.
- Michael Arbel, Anna Korba, Adil Salim, and Arthur Gretton. Maximum mean discrepancy gradient flow. *Advances in Neural Information Processing Systems*, 32, 2019.
- W. Arendt. Generators of positive semigroups. In Franz Kappel and Wilhelm Schappacher (eds.), Infinite-Dimensional Systems, pp. 1–15, Berlin, Heidelberg, 1984. Springer. ISBN 978-3-540-38932-3.
- Souhaib Attaiki, Gautam Pai, and Maks Ovsjanikov. DPFM: Deep Partial Functional Maps. In *2021 International Conference on 3D Vision (3DV)*, pp. 175–185, London, United Kingdom, December 2021. IEEE. ISBN 978-1-66542-688-6.
- Mathieu Aubry, Ulrich Schlickewei, and Daniel Cremers. The wave kernel signature: A quantum mechanical approach to shape analysis. In *2011 IEEE International Conference on Computer Vision Workshops (ICCV Workshops)*, pp. 1626–1633, Barcelona, Spain, November 2011. IEEE. ISBN 978-1-4673-0063-6 978-1-4673-0062-9 978-1-4673-0061-2.
- Gavin Barill, Neil G. Dickson, Ryan Schmidt, David I. W. Levin, and Alec Jacobson. Fast winding numbers for soups and clouds. *ACM Transactions on Graphics*, 37(4):1–12, August 2018.
- M. Faisal Beg, Michael I. Miller, Alain Trouvé, and Laurent Younes. Computing Large Deformation Metric Mappings via Geodesic Flows of Diffeomorphisms. *International Journal of Computer Vision*, 61(2):139–157, February 2005.
- Jens Behley, Martin Garbade, Andres Milioto, Jan Quenzel, Sven Behnke, Cyrill Stachniss, and Jurgen Gall. SemanticKITTI: A Dataset for Semantic Scene Understanding of LiDAR Sequences. In *Proceedings of the IEEE/CVF International Conference on Computer Vision*, pp. 9297–9307, 2019.
- Maysam Behmanesh, Maximilian Krahn, and Maks Ovsjanikov. TIDE: Time Derivative Diffusion for Deep Learning on Graphs. In *Proceedings of the 40th International Conference on Machine Learning*, pp. 2015–2030. PMLR, July 2023.
- Mikhail Belkin, Jian Sun, and Yusu Wang. Constructing Laplace Operator from Point Clouds in \mathbb{R}^d . In *Proceedings of the Twentieth Annual ACM-SIAM Symposium on Discrete Algorithms*, pp. 1031–1040. Society for Industrial and Applied Mathematics, January 2009. ISBN 978-0-89871-680-1 978-1-61197-306-8.
- Abraham Berman and Robert J. Plemmons. *Nonnegative Matrices in the Mathematical Sciences*.
 Classics in Applied Mathematics. Society for Industrial and Applied Mathematics, January 1994. ISBN 978-0-89871-321-3.
 - Alexander I. Bobenko and Boris A. Springborn. A Discrete Laplace–Beltrami Operator for Simplicial Surfaces. *Discrete & Computational Geometry*, 38(4):740–756, December 2007.

- Federica Bogo, Javier Romero, Matthew Loper, and Michael J. Black. FAUST: Dataset and Evaluation for 3D Mesh Registration. In *Proceedings of the IEEE Conference on Computer Vision and Pattern Recognition*, pp. 3794–3801, 2014.
 - Federica Bogo, Javier Romero, Gerard Pons-Moll, and Michael J. Black. Dynamic FAUST: Registering Human Bodies in Motion. In 2017 IEEE Conference on Computer Vision and Pattern Recognition (CVPR), pp. 5573–5582, Honolulu, HI, July 2017. IEEE. ISBN 978-1-5386-0457-1.
 - Alexandre Bône, Maxime Louis, Benoît Martin, and Stanley Durrleman. Deformetrica 4: an open-source software for statistical shape analysis. In *Shape in medical imaging: international work-shop, ShapeMI 2018, held in conjunction with MICCAI 2018, granada, Spain, september 20, 2018, proceedings*, pp. 3–13. Springer, 2018.
 - F.L. Bookstein. Principal warps: Thin-plate splines and the decomposition of deformations. *IEEE Transactions on Pattern Analysis and Machine Intelligence*, 11(6):567–585, June 1989.
 - Mario Botsch, Leif Kobbelt, Mark Pauly, Pierre Alliez, and Bruno Lévy. *Polygon Mesh Processing*. AK Peters / CRC Press, September 2010. ISBN 978-1-56881-426-1.
 - Michael M. Bronstein and Iasonas Kokkinos. Scale-invariant heat kernel signatures for non-rigid shape recognition. In 2010 IEEE Computer Society Conference on Computer Vision and Pattern Recognition, pp. 1704–1711, San Francisco, CA, USA, June 2010. IEEE. ISBN 978-1-4244-6984-0.
 - Michael M Bronstein, Joan Bruna, Taco Cohen, and Petar Veličković. Geometric Deep Learning: Grids, Groups, Graphs, Geodesics, and Gauges. *arXiv preprint arXiv:2104.13478*, 2021.
 - Dongliang Cao, Paul Roetzer, and Florian Bernard. Unsupervised Learning of Robust Spectral Shape Matching. *ACM Transactions on Graphics*, 42(4):132:1–132:15, July 2023.
 - Dongliang Cao, Zorah Lähner, and Florian Bernard. Synchronous Diffusion for Unsupervised Smooth Non-rigid 3D Shape Matching. In Aleš Leonardis, Elisa Ricci, Stefan Roth, Olga Russakovsky, Torsten Sattler, and Gül Varol (eds.), *Computer Vision ECCV 2024*, volume 15063, pp. 262–281. Springer Nature Switzerland, Cham, 2025. ISBN 978-3-031-72651-4 978-3-031-72652-1.
 - Ben Chamberlain, James Rowbottom, Maria I. Gorinova, Michael Bronstein, Stefan Webb, and Emanuele Rossi. GRAND: Graph Neural Diffusion. In *Proceedings of the 38th International Conference on Machine Learning*, pp. 1407–1418. PMLR, July 2021.
 - Benjamin Charlier, Jean Feydy, Joan Alexis Glaunès, François-David Collin, and Ghislain Durif. Kernel operations on the GPU, with autodiff, without memory overflows. *J. Mach. Learn. Res.*, 22(1):74:3457–74:3462, January 2021.
 - Xiuyuan Cheng and Boris Landa. Bi-stochastically normalized graph Laplacian: Convergence to manifold Laplacian and robustness to outlier noise. *Information and Inference: A Journal of the IMA*, 13(4):iaae026, December 2024.
 - F. R. K. Chung. Spectral Graph Theory. American Mathematical Society, 1997.
 - Ronald R. Coifman and Stéphane Lafon. Diffusion maps. *Applied and Computational Harmonic Analysis*, 21(1):5–30, July 2006.
 - Keenan Crane. Discrete differential geometry: An applied introduction. *Notices of the AMS, Communication*, 1153, 2018.
- Keenan Crane. The n-dimensional cotangent formula. *Online note. URL: https://www. cs. cmu. edu/~kmcrane/Projects/Other/nDCotanFormula. pdf*, pp. 11–32, 2019.
 - Keenan Crane, Clarisse Weischedel, and Max Wardetzky. The heat method for distance computation. *Communications of the ACM*, 60(11):90–99, October 2017.
 - Marco Cuturi. Sinkhorn Distances: Lightspeed Computation of Optimal Transport. *Advances in Neural Information Processing Systems*, 26, 2013.

- Tri Dao. FlashAttention-2: Faster Attention with Better Parallelism and Work Partitioning. In *The Twelfth International Conference on Learning Representations*, October 2023.
 - Nicolas Donati, Abhishek Sharma, and Maks Ovsjanikov. Deep Geometric Functional Maps: Robust Feature Learning for Shape Correspondence. In 2020 IEEE/CVF Conference on Computer Vision and Pattern Recognition (CVPR), pp. 8589–8598, Seattle, WA, USA, June 2020. IEEE. ISBN 978-1-72817-168-5.
 - Stanley Durrleman, Marcel Prastawa, Nicolas Charon, Julie R. Korenberg, Sarang Joshi, Guido Gerig, and Alain Trouvé. Morphometry of anatomical shape complexes with dense deformations and sparse parameters. *NeuroImage*, 101:35–49, November 2014.
 - Klaus-Jochen Engel, Rainer Nagel, and Simon Brendle. *One-parameter semigroups for linear evolution equations*, volume 194. Springer, 2000.
 - Nicole Feng and Keenan Crane. A Heat Method for Generalized Signed Distance. *ACM Transactions on Graphics*, 43(4):1–19, July 2024.
 - Jean Feydy, Thibault Séjourné, François-Xavier Vialard, Shun-ichi Amari, Alain Trouve, and Gabriel Peyré. Interpolating between Optimal Transport and MMD using Sinkhorn Divergences. In *Proceedings of the Twenty-Second International Conference on Artificial Intelligence and Statistics*, pp. 2681–2690. PMLR, April 2019.
 - Jean Feydy, Alexis Glaunès, Benjamin Charlier, and Michael Bronstein. Fast geometric learning with symbolic matrices. In *Advances in Neural Information Processing Systems*, volume 33, pp. 14448–14462. Curran Associates, Inc., 2020.
 - Matthew Fisher, Boris Springborn, TU Berlin, and Peter Schroder. An Algorithm for the Construction of Intrinsic Delaunay Triangulations with Applications to Digital Geometry Processing. *Discrete Differential Geometry*, 2006.
 - Sylvestre Gallot, Dominique Hulin, and Jacques Lafontaine. *Riemannian Geometry*. Universitext. Springer, Berlin, Heidelberg, 2004. ISBN 978-3-540-20493-0 978-3-642-18855-8.
 - Alexander Gao, Maurice Chu, Mubbasir Kapadia, Ming C. Lin, and Hsueh-Ti Derek Liu. An intrinsic vector heat network. In *Proceedings of the 41st International Conference on Machine Learning*, volume 235 of *ICML*'24, pp. 14638–14650, Vienna, Austria, July 2024. JMLR.org.
 - Justin Gilmer, Samuel S. Schoenholz, Patrick F. Riley, Oriol Vinyals, and George E. Dahl. Neural Message Passing for Quantum Chemistry. In *Proceedings of the 34th International Conference* on Machine Learning, pp. 1263–1272. PMLR, July 2017.
 - Eitan Grinspun, Anil N. Hirani, Mathieu Desbrun, and Peter Schröder. Discrete shells. In *Proceedings of the 2003 ACM SIGGRAPH/Eurographics Symposium on Computer Animation*, SCA '03, pp. 62–67, Goslar, DEU, July 2003. Eurographics Association. ISBN 978-1-58113-659-3.
 - Will Hamilton, Zhitao Ying, and Jure Leskovec. Inductive Representation Learning on Large Graphs. In *Advances in Neural Information Processing Systems*, volume 30. Curran Associates, Inc., 2017.
 - Roger A. Horn and Charles R. Johnson. *Matrix Analysis*. Cambridge University Press, Cambridge, 1985.
 - Yuanming Hu, Tzu-Mao Li, Luke Anderson, Jonathan Ragan-Kelley, and Frédo Durand. Taichi: a language for high-performance computation on spatially sparse data structures. *ACM Transactions on Graphics (TOG)*, 38(6):201, 2019.
- Bernhard Kerbl, Georgios Kopanas, Thomas Leimkuehler, and George Drettakis. 3D Gaussian Splatting for Real-Time Radiance Field Rendering. *ACM Transactions on Graphics*, 42(4):139:1–139:14, July 2023.
 - Martin Kilian, Niloy J. Mitra, and Helmut Pottmann. Geometric modeling in shape space. *ACM Trans. Graph.*, 26(3):64–es, July 2007.

- Thomas N. Kipf and Max Welling. Semi-Supervised Classification with Graph Convolutional Networks. In *International Conference on Learning Representations*, February 2017.
 - Philip A. Knight, Daniel Ruiz, and Bora Uçar. A Symmetry Preserving Algorithm for Matrix Scaling. *SIAM Journal on Matrix Analysis and Applications*, 35(3):931–955, January 2014.
 - Anna Korba, Francis Bach, and Clémentine Chazal. Statistical and geometrical properties of the kernel Kullback-Leibler divergence. *Advances in Neural Information Processing Systems*, 37: 32536–32569, 2024.
 - Venkat Krishnamurthy and Marc Levoy. Fitting smooth surfaces to dense polygon meshes. In *Proceedings of the 23rd annual conference on Computer graphics and interactive techniques*, pp. 313–324, 1996.
 - J.-O. Lachaud, D. Coeurjolly, C. Labart, P. Romon, and B. Thibert. Lightweight Curvature Estimation on Point Clouds with Randomized Corrected Curvature Measures. *Computer Graphics Forum*, 42(5):e14910, 2023.
 - Benjamin Lefaudeux, Francisco Massa, Diana Liskovich, Wenhan Xiong, Vittorio Caggiano, Sean Naren, Min Xu, Jieru Hu, Marta Tintore, Susan Zhang, Patrick Labatut, Daniel Haziza, Luca Wehrstedt, Jeremy Reizenstein, and Grigory Sizov. xformers: A modular and hackable transformer modelling library. https://github.com/facebookresearch/xformers, 2022.
 - B. Levy. Laplace-Beltrami Eigenfunctions Towards an Algorithm That "Understands" Geometry. In *IEEE International Conference on Shape Modeling and Applications 2006 (SMI'06)*, pp. 13–13, Matsushima, Japan, 2006. IEEE. ISBN 978-0-7695-2591-4.
 - Qiang Liu and Dilin Wang. Stein variational gradient descent: A general purpose Bayesian inference algorithm. *Advances in neural information processing systems*, 29, 2016.
 - Daniel S. Marcus, Tracy H. Wang, Jamie Parker, John G. Csernansky, John C. Morris, and Randy L. Buckner. Open Access Series of Imaging Studies (OASIS): Cross-sectional MRI data in young, middle aged, nondemented, and demented older adults. *Journal of Cognitive Neuroscience*, 19 (9):1498–1507, September 2007.
 - Nicholas F Marshall and Ronald R Coifman. Manifold learning with bi-stochastic kernels. *IMA Journal of Applied Mathematics*, 84(3):455–482, 2019.
 - S. Melzi, R. Marin, E. Rodolà, U. Castellani, J. Ren, A. Poulenard, P. Wonka, and M. Ovsjanikov. *Matching Humans with Different Connectivity*. The Eurographics Association, 2019. ISBN 978-3-03868-077-2.
 - Mark Meyer, Mathieu Desbrun, Peter Schröder, and Alan H. Barr. Discrete Differential-Geometry Operators for Triangulated 2-Manifolds. In Gerald Farin, Hans-Christian Hege, David Hoffman, Christopher R. Johnson, Konrad Polthier, Hans-Christian Hege, and Konrad Polthier (eds.), *Visualization and Mathematics III*, pp. 35–57. Springer Berlin Heidelberg, Berlin, Heidelberg, 2003. ISBN 978-3-642-05682-6 978-3-662-05105-4.
 - Mario Micheli, Peter W Michor, and David Mumford. Sectional curvature in terms of the cometric, with applications to the Riemannian manifolds of landmarks. *SIAM Journal on Imaging Sciences*, 5(1):394–433, 2012.
 - Baptiste Nicolet, Alec Jacobson, and Wenzel Jakob. Large steps in inverse rendering of geometry. *ACM Transactions on Graphics*, 40(6):1–13, December 2021.
 - Maks Ovsjanikov, Mirela Ben-Chen, Justin Solomon, Adrian Butscher, and Leonidas Guibas. Functional maps: A flexible representation of maps between shapes. *ACM Transactions on Graphics*, 31(4):1–11, August 2012.
 - F. Pedregosa, G. Varoquaux, A. Gramfort, V. Michel, B. Thirion, O. Grisel, M. Blondel, P. Prettenhofer, R. Weiss, V. Dubourg, J. Vanderplas, A. Passos, D. Cournapeau, M. Brucher, M. Perrot, and E. Duchesnay. Scikit-learn: Machine learning in Python. *Journal of Machine Learning Research*, 12:2825–2830, 2011.

- Xavier Pennec, Stefan Sommer, and Tom Fletcher. Riemannian geometric statistics in medical image analysis. Academic Press, 2019.
- Gabriel Peyré, Marco Cuturi, et al. Computational optimal transport: With applications to data science. *Foundations and Trends*® *in Machine Learning*, 11(5-6):355–607, 2019.
 - Ulrich Pinkall and Konrad Polthier. Computing Discrete Minimal Surfaces and Their Conjugates. *Experimental Mathematics*, 2(1):15–36, January 1993.
 - Jing Ren, Adrien Poulenard, Peter Wonka, and Maks Ovsjanikov. Continuous and orientation-preserving correspondences via functional maps. *ACM Transactions on Graphics*, 37(6):1–16, January 2019.
 - Martin Reuter, Franz-Erich Wolter, and Niklas Peinecke. Laplace–Beltrami spectra as 'Shape-DNA' of surfaces and solids. *Computer-Aided Design*, 38(4):342–366, April 2006.
 - Maria L Rizzo and Gábor J Székely. Energy distance. wiley interdisciplinary reviews: Computational statistics, 8(1):27–38, 2016.
 - Yousef Saad. *Numerical Methods for Large Eigenvalue Problems*. Classics in Applied Mathematics. Society for Industrial and Applied Mathematics, January 2011. ISBN 978-1-61197-072-2.
 - Josua Sassen, Henrik Schumacher, Martin Rumpf, and Keenan Crane. Repulsive Shells. *ACM Transactions on Graphics*, 43(4):1–22, July 2024.
 - Helmut H. Schaefer. *Banach Lattices and Positive Operators*. Springer, Berlin, Heidelberg, 1974. ISBN 978-3-642-65972-0 978-3-642-65970-6.
 - Nicholas Sharp and Keenan Crane. A Laplacian for Nonmanifold Triangle Meshes. *Computer Graphics Forum*, 39(5):69–80, August 2020.
 - Nicholas Sharp, Yousuf Soliman, and Keenan Crane. Navigating intrinsic triangulations. *ACM Transactions on Graphics*, 38(4):1–16, August 2019a.
 - Nicholas Sharp, Yousuf Soliman, and Keenan Crane. The Vector Heat Method. *ACM Transactions on Graphics*, 38(3):1–19, June 2019b.
 - Nicholas Sharp, Souhaib Attaiki, Keenan Crane, and Maks Ovsjanikov. DiffusionNet: Discretization Agnostic Learning on Surfaces. *ACM Transactions on Graphics*, 41(3):1–16, June 2022.
 - Richard Sinkhorn and Paul Knopp. Concerning nonnegative matrices and doubly stochastic matrices. *Pacific Journal of Mathematics*, 21(2):343–348, May 1967.
 - Olga Sorkine. Laplacian Mesh Processing. In *Eurographics 2005 State of the Art Reports*. The Eurographics Association, 2005.
 - Olga Sorkine and Marc Alexa. As-rigid-as-possible surface modeling. In *Proceedings of the Fifth Eurographics Symposium on Geometry Processing*, SGP '07, pp. 109–116, Goslar, DEU, July 2007. Eurographics Association. ISBN 978-3-905673-46-3.
 - Jian Sun, Maks Ovsjanikov, and Leonidas Guibas. A Concise and Provably Informative Multi-Scale Signature Based on Heat Diffusion. *Computer Graphics Forum*, 28(5):1383–1392, July 2009.
 - G. Taubin. Curve and surface smoothing without shrinkage. In *Proceedings of IEEE International Conference on Computer Vision*, pp. 852–857, June 1995.
 - Petar Veličković, Guillem Cucurull, Arantxa Casanova, Adriana Romero, Pietro Liò, and Yoshua Bengio. Graph Attention Networks. In *International Conference on Learning Representations*, February 2018.
 - Matthias Vestner, Zorah Lähner, Amit Boyarski, Or Litany, Ron Slossberg, Tal Remez, Emanuele Rodola, Alex Bronstein, Michael Bronstein, Ron Kimmel, and Daniel Cremers. Efficient Deformable Shape Correspondence via Kernel Matching. In 2017 International Conference on 3D Vision (3DV), pp. 517–526, October 2017.

- Pauli Virtanen, Ralf Gommers, Travis E. Oliphant, Matt Haberland, Tyler Reddy, David Cournapeau, Evgeni Burovski, Pearu Peterson, Warren Weckesser, Jonathan Bright, Stéfan J. van der Walt, Matthew Brett, Joshua Wilson, K. Jarrod Millman, Nikolay Mayorov, Andrew R. J. Nelson, Eric Jones, Robert Kern, Eric Larson, C J Carey, İlhan Polat, Yu Feng, Eric W. Moore, Jake VanderPlas, Denis Laxalde, Josef Perktold, Robert Cimrman, Ian Henriksen, E. A. Quintero, Charles R. Harris, Anne M. Archibald, Antônio H. Ribeiro, Fabian Pedregosa, Paul van Mulbregt, and SciPy 1.0 Contributors. SciPy 1.0: Fundamental Algorithms for Scientific Computing in Python. *Nature Methods*, 17:261–272, 2020. doi: 10.1038/s41592-019-0686-2.
- Ulrike von Luxburg. A tutorial on spectral clustering. *Statistics and Computing*, 17(4):395–416, December 2007.
- Max Wardetzky, Saurabh Mathur, Felix Kälberer, and Eitan Grinspun. Discrete Laplace operators: No free lunch. In *ACM SIGGRAPH ASIA 2008 Courses on SIGGRAPH Asia '08*, pp. 1–5, Singapore, 2008. ACM Press.
- Caroline L Wormell and Sebastian Reich. Spectral convergence of diffusion maps: Improved error bounds and an alternative normalization. *SIAM Journal on Numerical Analysis*, 59(3):1687–1734, 2021.
- Wenxuan Wu, Zhongang Qi, and Li Fuxin. PointConv: Deep Convolutional Networks on 3D Point Clouds. In 2019 IEEE/CVF Conference on Computer Vision and Pattern Recognition (CVPR), pp. 9613–9622, June 2019.
- Ling Yang, Zhilong Zhang, Yang Song, Shenda Hong, Runsheng Xu, Yue Zhao, Wentao Zhang, Bin Cui, and Ming-Hsuan Yang. Diffusion models: A comprehensive survey of methods and applications. *ACM Computing Surveys*, 56(4):1–39, 2023.
- Hongyu Zhou and Zorah Lähner. Laplace-Beltrami Operator for Gaussian Splatting. *arXiv preprint arXiv:2502.17531*, 2025.

CONTINUOUS FORMULATION OF THE METZLER CONDITION

Let A be a real square matrix. We say that A is a *Metzler* matrix if its off-diagonal entries are non-negative. This condition implies that the matrix exponential e^{tA} has non-negative entries for all $t \ge 0$. To see this, remark that for t close enough to 0, we have $e^{tA} = I + tA + o(t)$. This implies that the diagonal coefficients are approximately 1, and the off-diagonal ones are approximately $tA_{ij} \ge 0$. Since for any t we have $e^{tA} = (e^{tA/P})^P$, we can take P large enough such that $e^{tA/P}$ is non-negative (by the small-t argument). Since matrix multiplication preserves non-negativity, e^{tA} is non-negative for all $t \geq 0$.

Reciprocally, if B is a matrix admitting a logarithm log(B) such that $B^t = exp(log(B)t)$ is entrywise positive for all $t \ge 0$, then the identity $B^t = I + t \log(B) + o(t)$ for small t shows that $\log(B)$ is a Metzler matrix.

To extend this reasoning beyond finite-dimensional spaces, we use the formalism of semigroups on Banach spaces (Engel et al., 2000):

Definition A.1. Let $T: t \to T(t)$ be a continuous function from \mathbb{R} to the space of bounded linear operators on a Banach space V. We say that T is a strongly continuous semigroup if:

- $\begin{array}{ll} (ii) & T(t+s) = T(t)T(s) \ \textit{for all} \ t, s \geq 0 \\ (iii) & \lim_{t \to 0} T(t)f = f \ \textit{for all} \ f \in V \end{array}$

Its generator A is defined on the set of signals $f \in V$ for which the limit exists as:

$$Af = \lim_{t \to 0} \frac{T(t)f - f}{t} \tag{6}$$

The semigroup is said to be positive if $T(t) f \ge 0$ for all $f \ge 0$ and $t \ge 0$.

Under this framework, a Metzler matrix A is the generator of a positive semigroup $t \mapsto e^{tA}$.

In full generality, extending the Metzler condition to infinite-dimensional operators is not straightforward since the notion of "off-diagonal" terms is ill-defined. The correct formalism uses Banach lattices; we refer to (Schaefer, 1974) for proper statements and (Arendt, 1984) for proofs. In our case, we make a simplifying assumption and restrict ourselves to Hilbert spaces of the form $L^2_{\mu}(\mathcal{X})$, which include both finite-dimensional Euclidean spaces and infinite-dimensional L^2 spaces. For any signal $f \in L^2_u(\mathcal{X})$, we define sign(f) pointwise as:

$$sign(f)(x) = \begin{cases} +1 & \text{if } f(x) > 0\\ -1 & \text{if } f(x) < 0 \text{ , so that } |f| = sign(f)f. \end{cases}$$
 (7)

This leads to the following proposition, which characterizes the Metzler property on general $L^2_{\nu}(\mathcal{X})$ spaces via a pointwise inequality:

Proposition A.1. Let $A: \mathbb{R}^N \to \mathbb{R}^N$ be a be a linear operator represented by a matrix. Then the following inequalities are equivalent:

- (Metzler condition) $A_{ij} \geq 0$ whenever $i \neq j$ (Kato's inequality) $A|f| \geq \operatorname{sign}(f) Af$ for all $f \in V$

Proof. Statement (ii) can be rewritten as: for all i,

$$\sum_{j} A_{ij} |f_j| \geq \operatorname{sign}(f_i) \sum_{j} A_{ij} f_j.$$
 (8)

If (i) holds, then for $i \neq j$ we have $A_{ij}|f_j| \geq A_{ij}f_j\operatorname{sign}(f_i)$, and, by definition, $A_{ii}|f_i| =$ $A_{ii}f_i \operatorname{sign}(f_i)$. Therefore we have Equation (8) and (ii).

Conversely, suppose (ii) holds. Consider a pair $i \neq j$ and a signal f such that $f_i = 1$, $f_j = -1$ and $f_k = 0$ for other indices k. Equation (8) implies that:

$$A_{ii} + A_{ij} \ge A_{ii} - A_{ij}$$
, i.e. $A_{ij} \ge 0$. (9)

This allows us to conclude.

865 866 867

868

870

871

872

873

874 875

876

877 878

879

880

881

882 883

884

885

886

887

889

890

891 892

893 894 895

896

897

898

899

900

901 902 903

904 905

906

907

908

909 910

911 912 913

914

915

916

917

864

We would like to extend the implication from the finite-dimensional case: if A satisfies Kato's inequality, then it should generate a semigroup of non-negative operators. In the infinite-dimensional setting, this implication requires additional structure.

Definition A.2. A strictly positive subeigenvector of an operator A is a function $f \in D(A)$ so that:

- $Af \leq \lambda f \text{ for some } \lambda \in \mathbb{R}$
- f > 0 almost everywhere

where D(A) denotes the domain of the (possibly unbounded) operator A.

This allows us to state the following result, which is a direct consequence of Theorem 1.7 in Arendt (1984):

Proposition A.2. Let A be a generator of a strongly continuous semigroup on $L^2_{\mu}(\mathcal{X})$. Assume that there exists a function $g \in D(A)$ such that:

- g is a strictly positive subeigenvector of $A^{\top \mu}$.
- (weak Kato's inequality) $\langle A^{\top_{\mu}}g, |f| \rangle_{\mu} \ge \langle \operatorname{sign}(f)Af, g \rangle_{\mu} \text{ for all } f \in D(A)$.

Then the semi-group is positive (see Definition A.1).

In our setting, the generator A is equal to the opposite $-\Delta$ of a Laplace-like operator, and q is the constant function 1. Since our set of axioms implies that $-\Delta^{\top}{}^{\mu}1 = -\Delta 1 = 0$, we always have that 1 is a strictly positive subeigenvector of $-\Delta^{\perp\mu}$. This allows us to propose the following definition of a Laplace-like operator, which generalizes Definition 4.1 to discrete measures:

Definition A.3 (General Laplace-like Operators). Let Δ be a generator of a strongly continuous semigroup on $L^2_{\mu}(\mathcal{X})$, where μ has finite total mass.

We say that Δ is a Laplace-like operator if for all $f \in L^2_\mu(\mathcal{X})$:

- (i)

- $\begin{array}{ll} \textit{Symmetry:} \ \Delta^{\top_{\mu}} = \Delta & (iii) & \textit{Positivity:} \ \langle f, \Delta f \rangle_{\mu} \geq 0 \\ \textit{Constant cancellation:} \ \Delta 1 = 0 & (iv) & \textit{Kato's inequality:} \ \langle \mathrm{sign}(f) \Delta f, 1 \rangle_{\mu} \geq 0 \end{array}$

The results above show that if $t \mapsto T(t)$ is the strongly continuous semigroup generated by such a Laplace-like operator Δ , then T(t) satisfies the conditions of a diffusion operator (Definition 4.2 in the main manuscript).

We note that the assumption of finite total mass for μ ensures that the constant function 1 belongs to $L_{\mu}^{2}(\mathcal{X})$, and that our definition includes, as a special case, the classical Laplace–Beltrami operator on compact Riemannian manifolds.

PROOF OF THEOREM 4.1

Our theoretical analysis relies on ideas developed in the context of entropy-regularized optimal transport. We refer to the standard textbook (Peyré et al., 2019) for a general introduction, and to Feydy et al. (2019) for precise statements of important lemmas. Let us now proceed with our proof of Theorem 4.1.

Proof. Recall that $\mu = \sum_{i=1}^{N} m_i \delta_{x_i}$ is a finite discrete measure with positive weights $m_i > 0$. The smoothing operator S can be written as the product:

$$S = KM, (10)$$

where K is a N-by-N symmetric matrix with positive coefficients $K_{ij} > 0$ and M = $\operatorname{diag}(m_1,\ldots,m_N)$ is a diagonal matrix. Our hypothesis of operator positivity on S implies that K is a positive semi-definite matrix. Finally, we can suppose that μ is a probability measure without loss of generality: going forward, we assume that $m_1 + \cdots + m_N = 1$.

Optimal Transport Formulation. We follow Eq. (1) in Feydy et al. (2019) and introduce the symmetric entropy-regularized optimal transport problem:

$$OT_{reg}(\mu, \mu) = \min_{\pi \in Plans(\mu, \mu)} \sum_{i,j=1}^{N} \pi_{ij} C_{ij} + KL(\pi, mm^{\top})$$
(11)

where $C_{ij} = -\log K_{ij}$ is the symmetric N-by-N cost matrix and Plans (μ, μ) is the simplex of N-by-N transport plans, i.e. non-negative matrices whose rows and columns sum up to $m = (m_1, \ldots, m_N)$. KL denotes the Kullback-Leibler divergence:

$$KL(\pi, mm^{\top}) = \sum_{i,j=1}^{N} \pi_{ij} \log \frac{\pi_{ij}}{m_i m_j}$$
 (12)

Compared with Feydy et al. (2019), we make the simplifying assumption that $\varepsilon = 1$ and do not require that $C_{ii} = 0$ on the diagonal since this hypothesis is not relevant to the lemmas that we use in our paper.

Sinkhorn Scaling. The above minimization problem is strictly convex. The fundamental result of entropy-regularized optimal transport, stated e.g. in Section 2.1 of Feydy et al. (2019) and derived from the Fenchel-Rockafellar theorem in convex optimization, is that its unique solution can be written as:

$$\pi_{ij} = \exp(f_i + g_j - C_{ij}) \, m_i m_j \,, \tag{13}$$

where $f=(f_1,\ldots,f_N)$ and $g=(g_1,\ldots,g_N)$ are two dual vectors, uniquely defined up to a common additive constant (a pair (f,g) is solution if and only if the pair (f-c,g+c) is also solution) – see Proposition 11 in Feydy et al. (2019). In our case, by symmetry, there exists a unique constant such that f=g – see Section B.3 in Feydy et al. (2019). We denote by $\ell=(\ell_1,\ldots,\ell_N)$ this unique "symmetric" solution. It is the unique vector such that:

$$\pi_{ij} = \exp(\ell_i + \ell_j - C_{ij}) m_i m_j = m_i e^{\ell_i} K_{ij} e^{\ell_j} m_j \tag{14}$$

is a valid transport plan in Plans (μ, μ) . This matrix is symmetric and such that for all i:

$$\sum_{j=1}^{N} \pi_{ij} = m_i \quad \text{i.e.} \quad e^{\ell_i} \sum_{j=1}^{N} K_{ij} e^{\ell_j} m_j = 1.$$
 (15)

We introduce the positive scaling coefficients $\lambda_i = e^{\ell_i}$, the diagonal scaling matrix $\Lambda = \text{diag}(\lambda_1, \dots, \lambda_N)$, and rewrite this equation as:

$$\Lambda KM\Lambda 1 = 1$$
 i.e. $Q1 = 1$ where $Q = \Lambda KM\Lambda$. (16)

This shows that scaling S = KM with Λ enforces our **constant preservation** axiom for diffusion operators – property (ii) in Definition 4.2. Likewise, since Λ is a diagonal matrix with positive coefficients, Q satisfies axioms (i) – **symmetry** with respect to M – and (iv) – **entrywise positivity**.

Crucially, Λ can be computed efficiently using a symmetrized Sinkhorn algorithm: our Algorithm 1 is directly equivalent to in Feydy et al. (2019, Eq. (25)).

Spectral Normalization. To conclude our proof, we now have to show that the normalized operator Q also satisfies axiom (iii) – **damping** – in our definition of diffusion operators, i.e. show that its eigenvalues all belong to the interval [0,1].

To this end, we first remark that $Q = \Lambda KM\Lambda = \Lambda K\Lambda M$ has the same eigenvalues as $Q' = \sqrt{M}\Lambda K\Lambda\sqrt{M}$, where $\sqrt{M} = \mathrm{diag}(\sqrt{m_1},\ldots,\sqrt{m_N})$. If α is a scalar and x is a vector, the eigenvalue equation:

$$Qx = \Lambda K \Lambda \sqrt{M} \underbrace{\sqrt{M} x}_{y} = \alpha x$$
 is equivalent to $Q'y = \sqrt{M} \Lambda K \Lambda \sqrt{M} y = \alpha y$ (17)

with the change of variables $y = \sqrt{M}x$.

Then, we remark that for any vector x in \mathbb{R}^N ,

$$\sum_{i,j=1}^{N} K_{ij} \lambda_i \lambda_j (\sqrt{m_j} x_i - \sqrt{m_i} x_j)^2$$
(18)

$$= \sum_{i,j=1}^{N} K_{ij} \lambda_i \lambda_j (m_j x_i^2 + m_i x_j^2 - 2\sqrt{m_i} \sqrt{m_j} x_i x_j)$$
 (19)

$$= \sum_{i=1}^{N} (\underbrace{\Lambda K M \Lambda 1}_{Q1=1})_{i} x_{i}^{2} + \sum_{j=1}^{N} (\underbrace{\Lambda K M \Lambda 1}_{Q1=1})_{j} x_{j}^{2} - 2 x^{\top} Q' x$$
 (20)

$$= 2x^{\mathsf{T}}(I - Q')x. \tag{21}$$

Since the upper term is non-negative as a sum of squares, we get that the eigenvalues of the symmetric matrix I - Q' are all non-negative. This implies that the eigenvalues of Q', and therefore the eigenvalues of Q, are bounded from above by 1.

In the other direction, recall that our hypothesis of operator positivity on S implies that K is a positive semi-definite matrix. This ensures that Q, and therefore Q, also have non-negative eigenvalues. Combining the two bounds, we show that the spectrum of the normalized operator Q is, indeed, included in the unit interval [0,1].

C Proof of Theorem 4.2

Proof. The hypotheses of our Theorem 4.2 fit perfectly with those of Theorem 1 in Feydy et al. (2019). Notably, we make the assumption that $\mathcal X$ is a bounded region of $\mathbb R^d$: we can replace it with a closed ball of finite radius, which is a compact metric space. Just as in Appendix B, we can assume without loss of generality that the finite measures μ^t and the limit measure μ are probability distributions, that sum up to 1: positive multiplicative constants are absorbed by the scaling coefficients Λ^t and Λ .

If k(x,y) is a Gaussian kernel of deviation $\sigma>0$, we use the cost function $\mathrm{C}(x,y)=\frac{1}{2}\|x-y\|^2$ and an entropic regularization parameter $\varepsilon=\sigma^2$. If k(x,y) is an exponential kernel at scale $\sigma>0$, the cost function is simply the Euclidean norm $\|x-y\|$ and the entropic regularization parameter ε is equal to σ .

Continuous Scaling Functions. The theory of entropy-regularized optimal transport allows us to interpret the dual variables f, g and ℓ of Eqs. (13-14) as continuous functions defined on the domain \mathcal{X} . Notably, for any probability distribution μ , the continuous function $\ell: \mathcal{X} \to \mathbb{R}$ is uniquely defined by the "Sinkhorn equation" – see Sections B.1 and B.3 in Feydy et al. (2019):

$$\forall x \in \mathcal{X}, \ \ell(x) = -\varepsilon \log \int_{\mathcal{X}} \exp \frac{1}{\varepsilon} (\ell(y) - C(x, y)) \, \mathrm{d}\mu(y) . \tag{22}$$

The first part of Theorem 4.2 is a reformulation of this standard result. We introduce the continuous, positive function:

$$\lambda(x) = \exp(\ell(x)/\varepsilon) > 0 \tag{23}$$

which is bounded on the compact domain \mathcal{X} . We remark that Eq. (22) now reads:

$$\forall x \in \mathcal{X}, \ \lambda(x) = \frac{1}{\int_{\mathcal{X}} k(x, y) \lambda(y) \, \mathrm{d}\mu(y)}$$
 (24)

i.e.
$$1 = \lambda(x) \int_{\mathcal{X}} k(x, y) \lambda(y) \, \mathrm{d}\mu(y)$$
. (25)

This implies that the operator Q defined in Equation (3) satisfies our **constant preservation** axiom for diffusion operators. By construction, it also satisfies the **symmetry** and **entrywise positivity** axioms. The **damping** property derives from the fact that we can write Q as the limit of the sequence of discrete diffusion operators Q^t with eigenvalues in [0,1].

Convergence. To prove it, note that the above discussion also applies to the discrete measures $\mu^t = \sum_{i=1}^{N_t} m_i^t \delta_{x_i^t}$. We can uniquely define a continuous function $\ell^t : \mathcal{X} \to \mathbb{R}$ such that:

$$\forall x \in \mathcal{X}, \ \ell^t(x) = -\varepsilon \log \sum_{j=1}^{N_t} m_j^t \exp \frac{1}{\varepsilon} \left(\ell^t(x_j^t) - C(x, x_j^t) \right), \tag{26}$$

and interpret the diagonal coefficients of the scaling matrix Λ^t as the values of the positive scaling function:

$$\lambda^t(x) = \exp(\ell^t(x)/\varepsilon) > 0 \tag{27}$$

sampled at locations $(x_1^t, \ldots, x_{N_t}^t)$.

Recall that the sequence of discrete measures μ^t converges weakly to μ as t tends to infinity. Crucially, Proposition 13 in Feydy et al. (2019) implies that the dual potentials ℓ^t converge uniformly on $\mathcal X$ towards ℓ . Since ℓ is continuous and therefore bounded on the compact domain $\mathcal X$, this uniform convergence also holds for the (exponentiated) scaling functions: λ^t converges uniformly on $\mathcal X$ towards λ .

For any continuous signal $f: \mathcal{X} \to \mathbb{R}$, we can write down the computation of $Q^t f$ as the composition of a pointwise multiplication with a scaled positive measure $\mu^t \lambda^t$, a convolution with the (fixed, continuous, bounded) kernel k, and a pointwise multiplication with the positive scaling function λ^t . In other words:

$$Q^t f = \lambda^t \cdot \left(k \star (\mu^t \lambda^t f) \right). \tag{28}$$

Likewise, we have that:

$$Qf = \lambda \cdot (k \star (\mu \lambda f)). \tag{29}$$

Since λ^t converges uniformly towards λ and f is continuous, the signed measure $\mu^t \lambda^t f$ converges weakly towards $\mu \lambda f$. This implies that the convolution with the (bounded) Gaussian or exponential kernel $k \star (\mu^t \lambda^t f)$ converges uniformly on \mathcal{X} towards $k \star (\mu \lambda f)$, which allows us to conclude. \square

D Q-DIFFUSION IN PRACTICE

Sinkhorn Convergence. We evaluate the convergence behavior of the symmetrized Sinkhorn algorithm across various settings. Specifically, we monitor the quantity:

$$\frac{\int \left|\Lambda^{(i)} S \Lambda^{(i)} 1 - 1\right| d\mu}{\int d\mu} \tag{30}$$

where $\Lambda^{(i)}$ denotes the diagonal scaling matrix after i Sinkhorn iterations. This corresponds to the average deviation between the constant signal 1 and its smoothed counterpart $Q^{(i)}1 = \Lambda^{(i)} S \Lambda^{(i)}1$ on the domain that is defined by the positive measure μ . According to our definition, both signals coincide when $Q^{(i)}$ is a smoothing operator. Figure 6 presents these results, with visualizations of the input modalities along the top row and corresponding convergence curves below. In Figure 6a, we report results for different representations of the Armadillo shape used in the main paper: uniform point cloud samples on the surface and volume, as well as voxel-based representations of the boundary and interior. Figure 6b illustrates the behavior on Erdős–Rényi random graphs with edge probability p=0.2, and Figure 6c shows results on geometric graphs, where points are uniformly sampled in the unit square and edges are drawn between points within radius r=0.15.

Across all experiments, we observe rapid convergence: typically, 5 to 10 iterations are sufficient to reach error levels below $10^{-3}=0.1\%$. We note that one iteration of our algorithm corresponds to the classical symmetric normalization of graph Laplacians, which satisfies our constant preservation property up to a precision of 1% to 5%. From this perspective, we understand our work as a clarification of the literature on graph Laplacians. While most practitioners are used to working with approximate normalization, we provide a clear and affordable method to satisfy this natural axiom up to an arbitrary tolerance parameter. We argue that this is preferable to choosing between rowwise normalization (which guarantees the preservation of constant signals, but discards symmetry) and standard symmetric normalization (which makes a small but noticeable error on the preservation of constant signals).

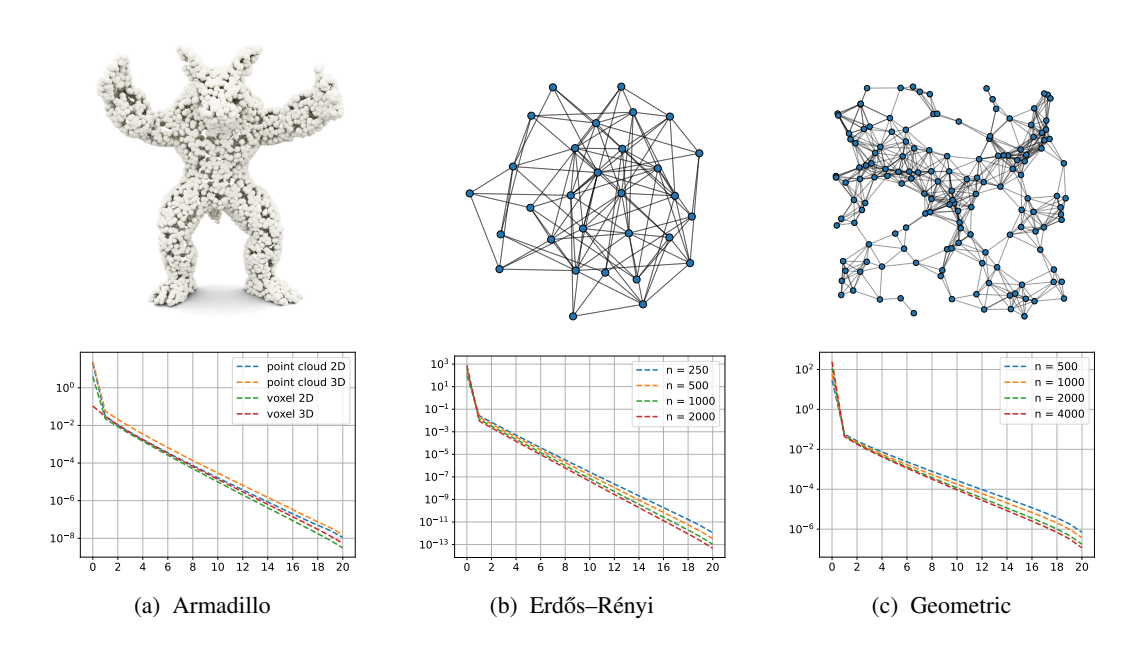


Figure 6: Convergence of the symmetric Sinkhorn algorithm on (a) the Armadillo shape, (b) a graph with N nodes and random edges, (c) a random geometric graph with N nodes

Implementing Q-Diffusion on Discrete Samples. Let $K \in \mathbb{R}^{N \times N}$ be a symmetric kernel matrix, and $M = \operatorname{diag}(m_1, \dots, m_N)$ be a diagonal mass matrix. As described in Algorithm 1, we compute a diagonal scaling matrix $\Lambda = \operatorname{diag}(e^{\ell_1}, \dots, e^{\ell_N})$, such that the normalized diffusion operator becomes $Q = \Lambda K M \Lambda$. This operator can be implemented efficiently using the KeOps library (Charlier et al., 2021; Feydy et al., 2020), which avoids instancing the dense kernel matrix.

In the case where K is a Gaussian kernel between points x_i in \mathbb{R}^d , with standard deviation $\sigma > 0$, applying Q to a signal $f \in \mathbb{R}^N$ gives:

$$(Qf)_{i} = \sum_{j=1}^{N} \exp\left(-\frac{1}{2\sigma^{2}} \|x_{i} - x_{j}\|^{2} + \ell_{i} + \ell_{j}\right) m_{j} f_{j}$$
(31)

$$= \sum_{j} \exp(q_{ij}) f_j \quad \text{where } q_{ij} := -\frac{1}{2\sigma^2} ||x_i - x_j||^2 + \ell_i + \ell_j + \log m_j. \tag{32}$$

Since Q is row-normalized by construction, (i.e., Q1=1), this operation can be written as a softmax-weighted sum:

$$(Qf)_i = \sum_{j=1}^{N} \operatorname{SoftMax}_j(q_{ij}) f_j.$$
(33)

We note that the scores q_{ij} can be expressed as inner products between extended embeddings $\tilde{x}_i, \tilde{y}_i \in \mathbb{R}^{d+2}$, enabling fast attention implementations:

$$q_{ij} = \tilde{x}_i^{\top} \tilde{y}_j$$
, where $\tilde{x}_i = \begin{pmatrix} \ell_i - \frac{\frac{1}{\sigma} x_i}{\frac{1}{2\sigma^2}} \|x_i\|^2 \\ 1 \end{pmatrix}$ and $\tilde{y}_j = \begin{pmatrix} \frac{\frac{1}{\sigma} x_j}{1} \\ \ell_j - \frac{1}{2\sigma^2} \|x_j\|^2 + \log(m_j) \end{pmatrix}$. (34)

This leads to an attention-style formulation of the operator:

$$Qf = Attention\left(\tilde{X}, \tilde{Y}, f\right) \tag{35}$$

where $\tilde{X}, \tilde{Y} \in \mathbb{R}^{N \times (d+2)}$ are the stacked embeddings of all points. This makes Qf compatible with fast attention layers such as FlashAttention (Dao, 2023) or xFormers (Lefaudeux et al., 2022). Note that the softmax normalization in the Attention layer is invariant to additive constants in \tilde{x}_i , allowing the implementation to be further simplified using only a (d+1)-dimensional embeddings for \tilde{X} and \tilde{Y}

Spectral Decomposition. The largest eigenvectors of a symmetric matrix can be efficiently computed using the power method or related iterative solvers (Saad, 2011). However, standard routines typically assume symmetry with respect to the standard inner product. Since our diffusion operator $Q = \Lambda KM\Lambda$ is symmetric with respect to the M-weighted inner product, we need to reformulate the problem. Noting that M and Λ are diagonal and therefore commute, we can write

$$Q = M^{-1} \left(\Lambda M K M \Lambda \right) . \tag{36}$$

This allows us to compute the eigenvectors and eigenvalues of Q by solving the following generalized eigenproblem for symmetric matrices:

$$(\Lambda MKM\Lambda)\Phi = \lambda M\Phi . \tag{37}$$

This is supported by standard linear algebra routines (such as scipy.sparse.linalg.eigsh) and ensures that the resulting eigenvectors Φ are orthogonal with respect to the M inner product.

E RUNTIMES

Setup. We time **5 iterations** of the symmetric Sinkhorn normalization on point-cloud kernels using PyTorch + PyKeOps (symbolic lazy tensors) on an NVIDIA V100 (CUDA 12.1). For reference, we also time implicit Laplacian diffusion via a sparse LU solve of $(M+t\Delta)$ on an Intel Xeon Gold 6248 CPU. This reflects typical usage: kernel mat-vecs map well to GPUs, whereas sparse direct solvers are mature and memory-efficient on CPUs when a Laplacian is available.

What is timed. Sinkhorn: each iteration = one mat-vec with S + a diagonal rescaling; we report wall-clock for 5 iterations. Laplacian: factorization + one solve of $(M+t\Delta)^{-1}b$ on CPU (best-case when a sparse Δ exists). Our GPU timings use a brute-force kernel on an unstructured 3D point cloud, and could be further improved.

Dense GPU baselines. On the GPU, we also measured a Cholesky factorization (210 ms) and a matrix exponential (770 ms) of a Laplacian in PyTorch and 10000 vertices. These approaches exceed GPU memory limits beyond \sim 10k points.

Sinkhorn Complexity. Per Sinkhorn iteration for different methods:

- (i) **Dense matrices** $S: O(N^2)$ time/memory
- (ii) **Symbolic kernel** S (e.g., Gaussian with PyKeOps): $O(N^2)$ time, O(N) memory sparse S (k-NN): O(kN) time (generally O(nnz))
- (iii) Low-rank (rank R): $O(RN^2)$
- (iv) **Grid convolution**: O(N) for small filters, $O(N \log N)$ for large filters using FFTs

Baseline Complexity. Per diffusion step via Laplacian-based methods:

- (i) Matrix exponential (dense): $O(N^3)$ time; rarely used at scale.
- (ii) Implicit Euler $(I+t\Delta)^{-1}$ with sparse LU/Cholesky: worst case $O(N^3)$; for mesh-like sparsity typically $O(N^{1.5})$ for factorization and $O(N^2)$ per solve (amortizable across right-hand sides).
- (iii) **Spectral truncation** (rank R): $O(RN^2)$ in the dense setting; truncation may introduce ringing artifacts.

These baselines assume access to a well-defined sparse Laplacian and specialized linear algebra routines.

F DETAILS ON EIGENVECTORS COMPUTATION

FEM Laplacian on Tetrahedral Meshes. In Figure 3 of the main paper, we implement our method on different representations of the Armadillo, treated as a surface and as a volume with

uniform density. For the surface mesh in Figure 3a, we use the standard cotangent Laplacian as a reference. For the tetrahedral mesh shown in Figure 3f, we use a finite element Laplacian, generalizing the cotangent Laplacian in 2D (Crane, 2019). Let $\{e_i\}$ be a basis of piecewise linear basis and $\{de_i\}$ their gradients. The discrete Laplacian Δ takes the form:

$$\Delta = M^{-1}L \,, \tag{38}$$

where L is the stiffness matrix and M is the mass matrix defined by:

$$L_{ij} = \langle de_i, de_j \rangle, \quad M_{ij} = \langle e_i, e_j \rangle.$$
 (39)

Following Crane (2019), we compute the off-diagonal entries of L with:

$$L_{ij} = \frac{1}{6} \sum_{ijkl \in \mathcal{T}} l_{kl} \cot(\theta_{kl}^{ij}), \qquad (40)$$

where \mathcal{T} is the set of tetrahedra in the mesh, l_{kl} is the length of edge kl, and θ_{kl}^{ij} is the dihedral angle between triangles ikl and jkl. The diagonal entries are defined to make sure that the rows sum to zero:

$$L_{ii} = -\sum_{j \neq i} L_{ij} . (41)$$

The entries of the mass matrix ${\cal M}$ are given by:

$$M_{ij} = \frac{1}{20} \sum_{ijkl \in \mathcal{T}} \text{vol}(ijkl) \text{ for } i \neq j , \quad M_{ii} = \frac{1}{10} \sum_{ijkl \in \mathcal{T}} \text{vol}(ijkl) .$$
 (42)

Point Clouds. As discussed in the main paper, we compare the eigendecompositions of these cotan Laplacians to that of our normalized Gaussian smoothings on discrete representations of the Armadillo. For the sake of simplicity, Figures 3b and 3g correspond to uniform discrete samples, i.e. weighted sums of Dirac masses:

$$\mu = \sum_{i=1}^{N} \frac{1}{N} \delta_{x_i} \,, \tag{43}$$

where x_1, \ldots, x_N correspond to N = 5000 three-dimensional points drawn at random on the triangle mesh (for Figure 3b) and in the tetrahedral volume (for Figure 3g).

Gaussian Mixtures. To compute the Gaussian mixture representations of Figures 3c and 3h, we simply rely on the Scikit-Learn implementation of the EM algorithm with K-Means++ initialization (Pedregosa et al., 2011) and 500 components. This allows us to write:

$$\mu = \sum_{i=1}^{500} m_i \mathcal{N}(x_i, \Sigma_i) , \qquad (44)$$

where the scalars m_i are the non-negative mixture weights, the points x_i are the Gaussian centroids and the 3-by-3 symmetric matrices Σ_i are their covariances.

Mass Estimation on Voxel Grids. To encode the Armadillo's *volume* as a binary mask in Figure 3i, we simply assign a mass of 1 to voxels that contain points inside of the watertight Armadillo surface. This allows us to demonstrate the robustness of our implementation, even when voxel values do not correspond to the exact volume of the intersection between the tetrahedral mesh and the cubic voxel.

However, this approach is too simplistic when representing the *surface* of the Armadillo with voxels. Since the grid is more densely sampled along the xyz axes than in other directions, assigning a uniform mass of 1 to every voxel that intersects the triangle mesh would lead to biased estimates of the mass distribution. To address this quantization issue, we use kernel density estimation to assign a mass m_i to each voxel.

As described above, we first turn the triangle mesh into a binary mask. Then, for every non-empty voxel x, we use an isotropic Gaussian kernel k with standard deviation σ equal to 3 voxels to estimate a voxel mass m(x) with:

$$m(x) = \frac{1}{\sum_{y} k(x, y)} \tag{45}$$

where the sum is taken over neighboring, non-empty voxels.

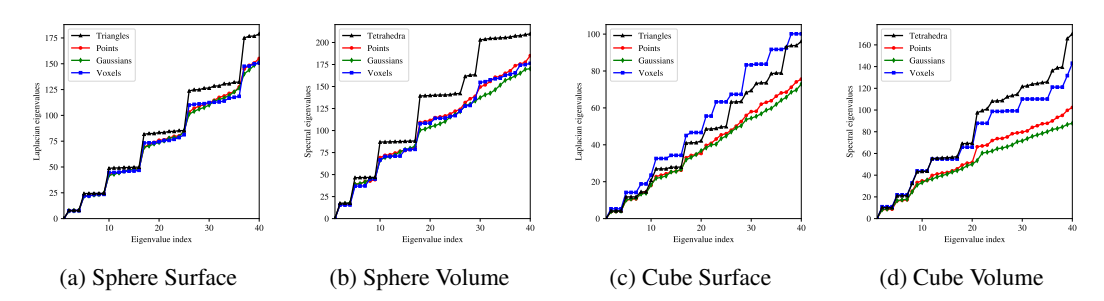


Figure 7: Laplacian eigenvalues for the sphere of diameter 1 and the cube of edge length 1.

Estimation of the Laplacian Eigenvalues. Recall that with our conventions, the Laplace operator is non-negative. In both of our settings (surface and volume), performing an eigendecomposition of the reference cotan Laplacian yields an *increasing* sequence of eigenvalues starting at $\lambda_1^{\Delta} = 0$. On the other hand, computing the largest eigenvalues of a normalized diffusion operator yields a *decreasing* sequence of eigenvalues starting at $\lambda_1^Q = 1$.

To compare both sequences with each other and produce the curves of Figure 3e and 3j, we propose the following simple heuristics for diffusions Q derived from a Gaussian kernel of deviation $\sigma > 0$:

• For point clouds and voxels, we use:

$$\lambda_i = -\frac{2}{\sigma^2} \log(\lambda_i^Q) \,. \tag{46}$$

Indeed, when the underlying measure μ corresponds to a regular grid with uniform weights, we can interpret the Gaussian kernel matrix as a convolution operator with a Gaussian kernel $\exp(-\|x\|^2/2\sigma^2)$. Its eigenvalues can be computed in the Fourier domain as $\exp(-\sigma^2\|\omega\|^2/2)$. To recover the eigenvalues $\|\omega\|^2$ of the Laplace operator, we simply have to apply a logarithm and multiply by $-2/\sigma^2$.

• For Gaussian mixtures with component weights m_i , centroids x_i and covariance matrices Σ_i , we use:

$$\lambda_i = -\frac{2}{\sigma^2 + \frac{2}{d}(\sum_i m_i \operatorname{trace}(\Sigma_i))/(\sum_i m_i)} \log(\lambda_i^Q), \qquad (47)$$

where d is equal to 2 for surfaces and 3 for volumes. This formula is easy to compute and introduces an additional factor, the average trace of the covariance matrices Σ_i . For volumes, it relies on the observation that when all covariance matrices are equal to a constant isotropic matrix $\Sigma = \tau^2 I_3$ with trace $3\tau^2$, the smoothing operator defined in Eq. (5) of the main paper is equivalent to a Gaussian kernel matrix of variance $\sigma^2 + 2\tau^2 = \sigma^2 + (2/3)\operatorname{trace}(\Sigma)$.

Likewise, for surfaces, we expect that a regular sampling will lead to covariance matrices that have one zero eigenvalue (in the normal direction) and two non-zero eigenvalues (in the tangent plane), typically equal to a constant τ^2 . This leads to the formula $\sigma^2 + 2\tau^2 = \sigma^2 + (2/2)\operatorname{trace}(\Sigma)$.

Estimated Spectrum on Standard Shapes. In Figures 8 and 9, we display the first 20 eigenvectors of our operators defined on the Armadillo, as a complement to Figure 3 in the main paper. As expected, these mostly coincide with each other.

Going further, we perform the exact same experiment with a sphere of diameter 1 in Figures 10 and 11, as well as a cube with edge length 1 in Figures 12 and 13. The relevant spectra are displayed in Figure 7. We recover the expected symmetries, which correspond to the plateaus in the spectra and the fact that the eigenvectors cannot be directly identified with each other. We deliberately choose coarse point cloud and Gaussian mixture representations, which allow us to test the robustness of our approach. Although the Laplacian eigenvalues tend to have a slower growth on noisy data, the eigenvectors remain qualitatively relevant.

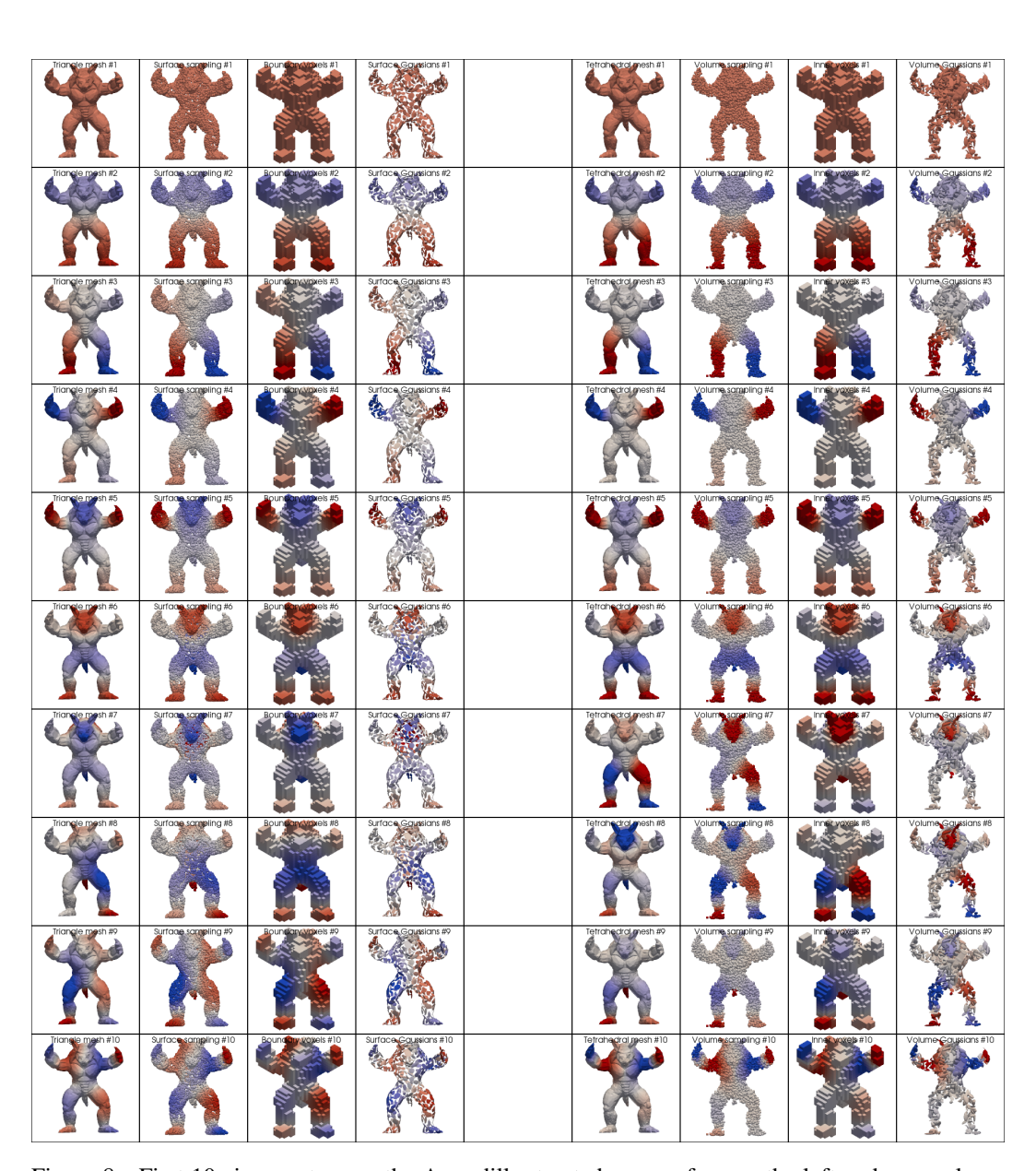


Figure 8: First 10 eigenvectors on the Armadillo, treated as a surface on the left and as a volume on the right. From left to right, the shape is encoded as a triangle mesh, a point cloud sampled uniformly at random, a voxel grid, a Gaussian mixture; a tetrahedral mesh, a point cloud, a binary mask and a Gaussian mixture. Figure 3 corresponds to the last row.

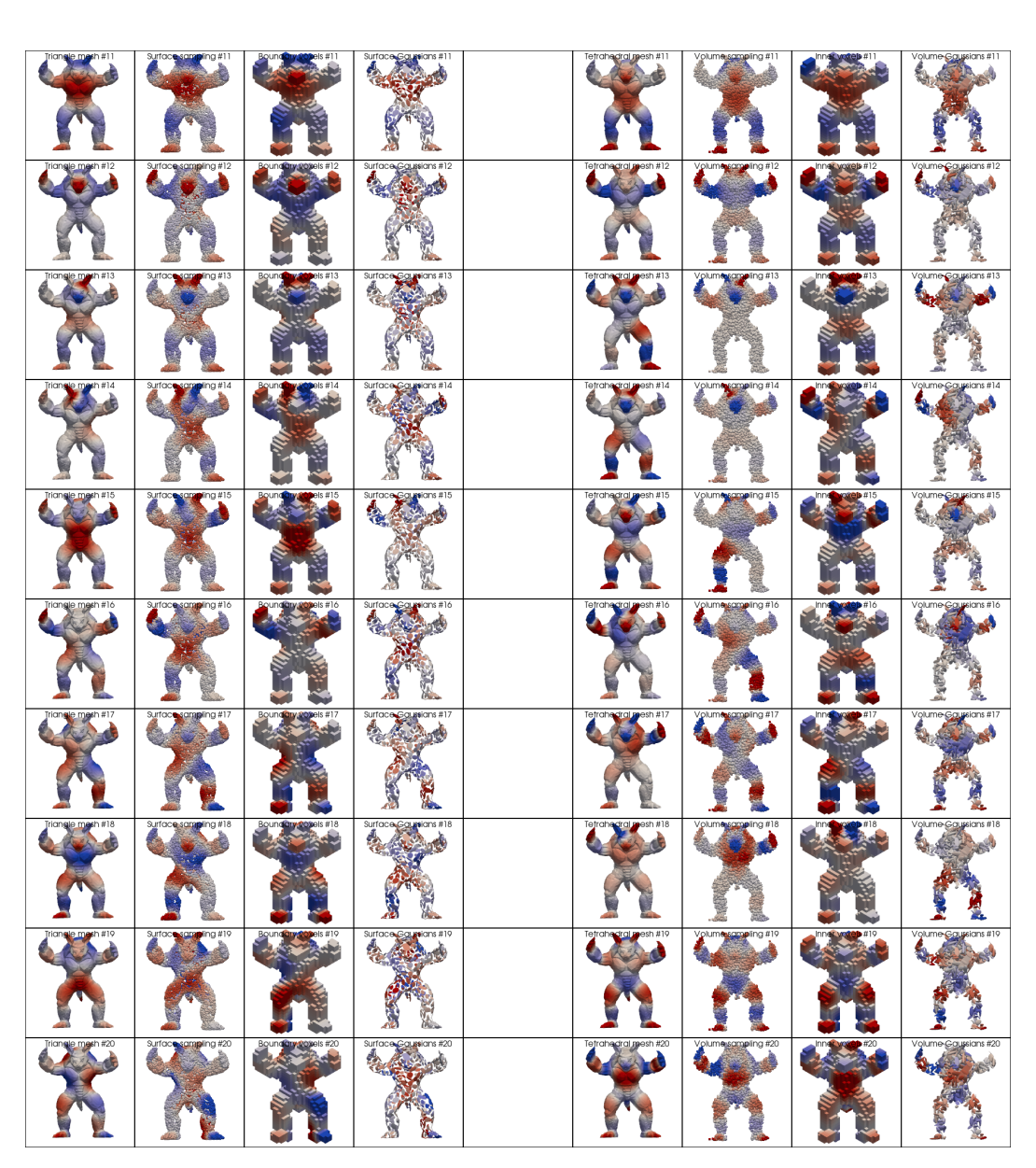


Figure 9: Eigenvectors 11 to 20 on the Armadillo, understood as a surface on the left and as a volume on the right. From left to right, the shape is encoded as a triangle mesh, a point cloud sampled uniformly at random, a voxel grid, a Gaussian mixture; a tetrahedral mesh, a point cloud, a binary mask and a Gaussian mixture.

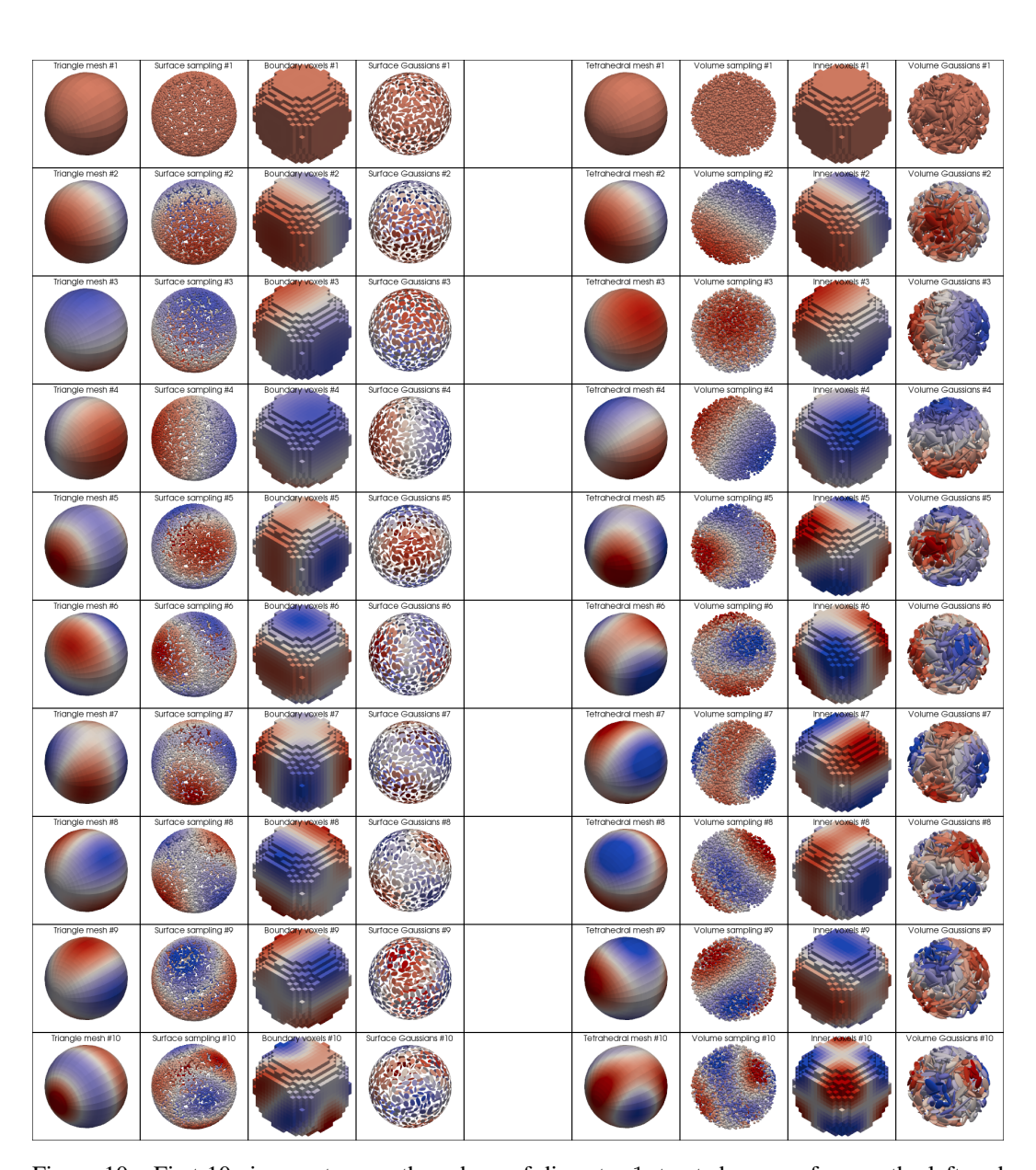


Figure 10: First 10 eigenvectors on the sphere of diameter 1, treated as a surface on the left and as a volume on the right. From left to right, the shape is encoded as a triangle mesh, a point cloud sampled uniformly at random, a voxel grid, a Gaussian mixture; a tetrahedral mesh, a point cloud, a binary mask and a Gaussian mixture.

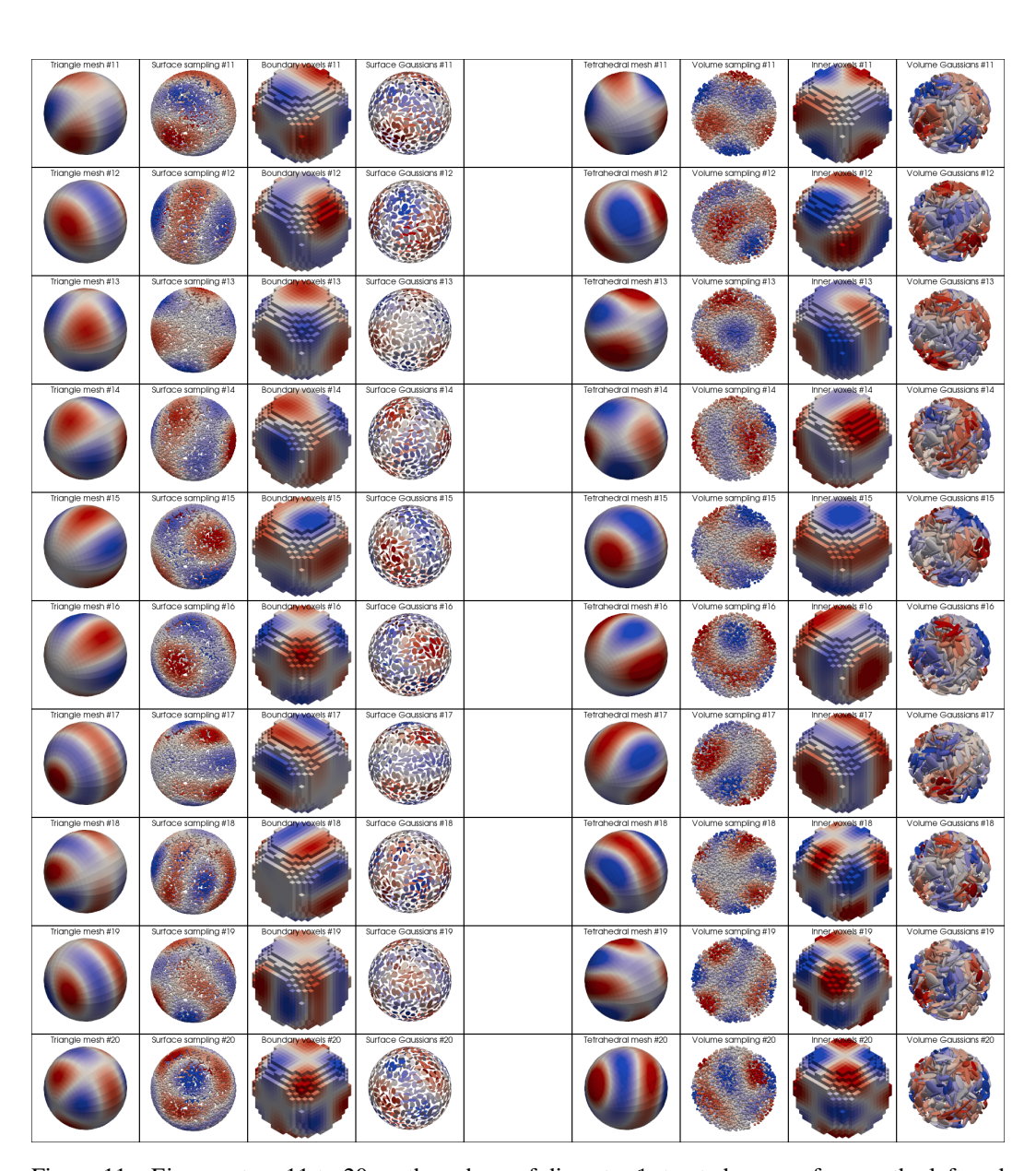


Figure 11: Eigenvectors 11 to 20 on the sphere of diameter 1, treated as a surface on the left and as a volume on the right. From left to right, the shape is encoded as a triangle mesh, a point cloud sampled uniformly at random, a voxel grid, a Gaussian mixture; a tetrahedral mesh, a point cloud, a binary mask and a Gaussian mixture.

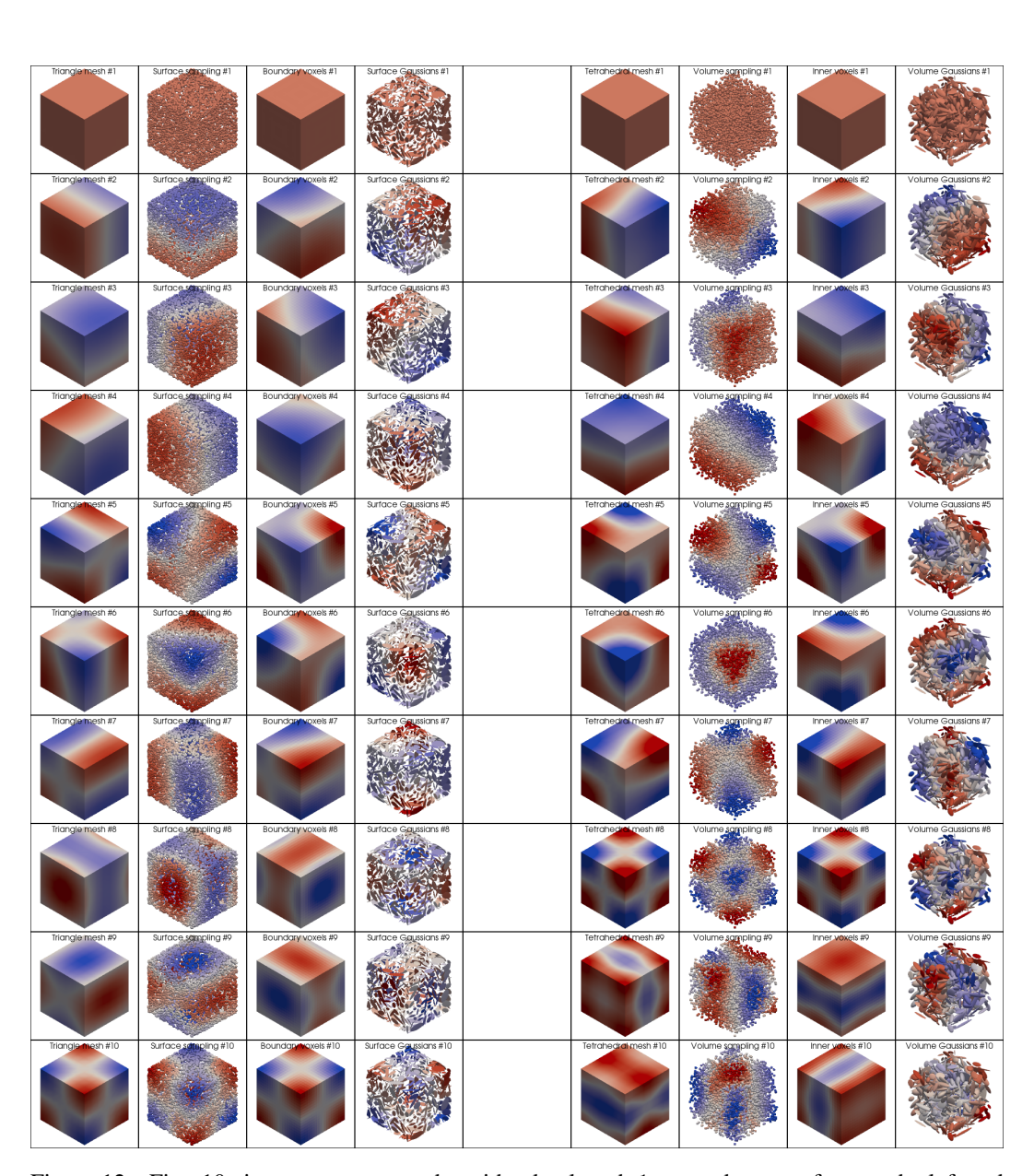


Figure 12: First 10 eigenvectors on a cube with edge length 1, treated as a surface on the left and as a volume on the right. From left to right, the shape is encoded as a triangle mesh, a point cloud sampled uniformly at random, a voxel grid, a Gaussian mixture; a tetrahedral mesh, a point cloud, a binary mask and a Gaussian mixture.

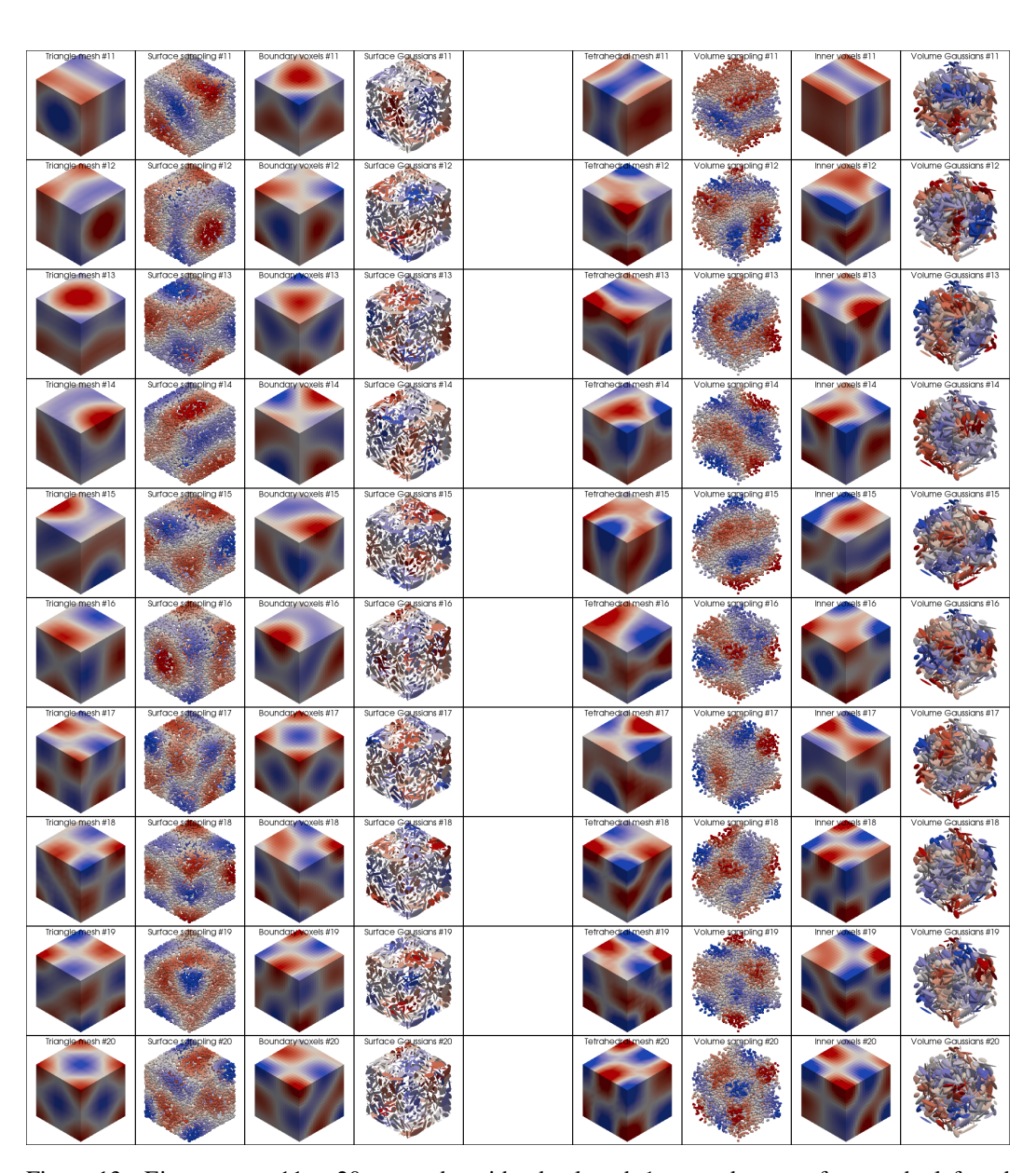


Figure 13: Eigenvectors 11 to 20 on a cube with edge length 1, treated as a surface on the left and as a volume on the right. From left to right, the shape is encoded as a triangle mesh, a point cloud sampled uniformly at random, a voxel grid, a Gaussian mixture; a tetrahedral mesh, a point cloud, a binary mask and a Gaussian mixture.

G DETAILS ON GRADIENT FLOW

The Energy Distance. Inspired by the theoretical literature on sampling and gradient flows, we perform a simple gradient descent experiment on the *Energy Distance* between two empirical distributions. Given a source (prior) distribution $\mu = \frac{1}{N} \sum_{i=1}^{N} \delta_{x_i}$ and a target distribution $\nu = \frac{1}{M} \sum_{j=1}^{M} \delta_{y_j}$, this loss function is defined as:

$$E(\mu, \nu) = \frac{1}{NM} \sum_{i}^{N} \sum_{j}^{M} \|x_i - y_j\| - \frac{1}{2N^2} \sum_{i,j=1}^{N} \|x_i - x_j\| - \frac{1}{2M^2} \sum_{i,j=1}^{M} \|y_i - y_j\|$$
(48)

When all points are distinct from each other, its gradient with respect to the positions of the source samples is:

$$\nabla_{x_i} E(\mu, \nu) = \frac{1}{NM} \sum_{j=1}^{M} \frac{y_j - x_i}{\|y_j - x_i\|} - \frac{1}{N^2} \sum_{j \neq i} \frac{x_j - x_i}{\|x_j - x_i\|}$$
(49)

We implement this formula efficiently using the KeOps library.

Particle Flow. Starting from point positions $x_i^{(0)}$, we then update the point positions iteratively using:

$$x_i^{(t+\eta)} \leftarrow x_i^{(t)} - \eta N L \nabla_{x_i^{(t)}} E\left(\frac{1}{N} \sum_{i=1}^N \delta_{x_i^{(t)}}, \nu\right),$$
 (50)

where L is an arbitrary linear operator and η is a positive step size. When L is the identity, this scheme corresponds to an explicit Euler integration of the Wasserstein gradient flow: Figure 14 is equivalent to classical simulations such as the first row of Figure 5 in Feydy et al. (2019).

Setup. Going further, we study the impact of different smoothing operators L that act as regularizers on the displacement field. We consider both unnormalized Gaussian kernel matrices and their normalized counterparts as choices for L, with standard deviation $\sigma=0.07$ in Figure 4 of the main paper and Figure 15, as well as $\sigma=0.2$ in a secondary experiment showcased in Figure 16. For each case, we run $T=1\,000$ iterations with a step size $\eta=0.05$.

Out of the box, unnormalized kernel matrices tend to aggregate many points and thus inflate gradients. To get comparable visualizations, we divide the unnormalized kernel matrix by the average of its row-wise sums at time t=0. This corresponds to an adjustment of the learning rate, which is not required for the descents with respect to the Wasserstein metric or with our normalized diffusion operators.

As a source distribution, we use a uniform sampling (N=1500) of a small rectangle in the unit square $[0,1]^2$. The target distribution is also sampled with M=1500 points using a reference image provided by the Geomloss library (Feydy et al., 2019). The entire optimization process takes a few seconds on a GeForce RTX 3060 Mobile GPU using KeOps for kernel computation.

Visualization. In Figure 14, we show a baseline gradient descent for the Wasserstein metric (L = I). As expected, the gradient flow heavily deforms the source distribution and leaves "stragglers" behind due to the vanishing gradient of the Energy Distance.

In Figure 15, we compare both kernel variants with $\sigma=0.07$ as in the main paper. In Figure 16, we use a larger standard deviation $\sigma=0.2$. In this case, the unregularized flow is more stable but still tends to overly contract the shape. In contrast, our normalized kernel consistently preserves the structural integrity of the source distribution.

H DETAILS ON NORMALIZED SHAPE METRICS

Hamiltonian Geodesic Shooting. To compute our shape geodesics, we implement the LDDMM framework on point clouds as done by the Deformetrica software (Bône et al., 2018). If (x_1, \ldots, x_N)

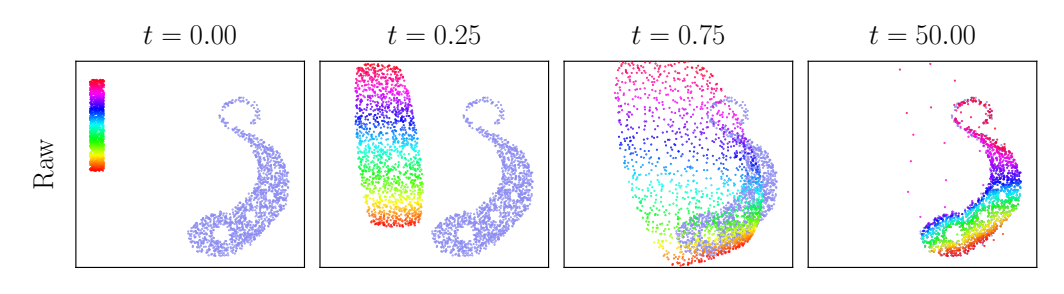


Figure 14: Gradient flow using the simple Wasserstein metric.

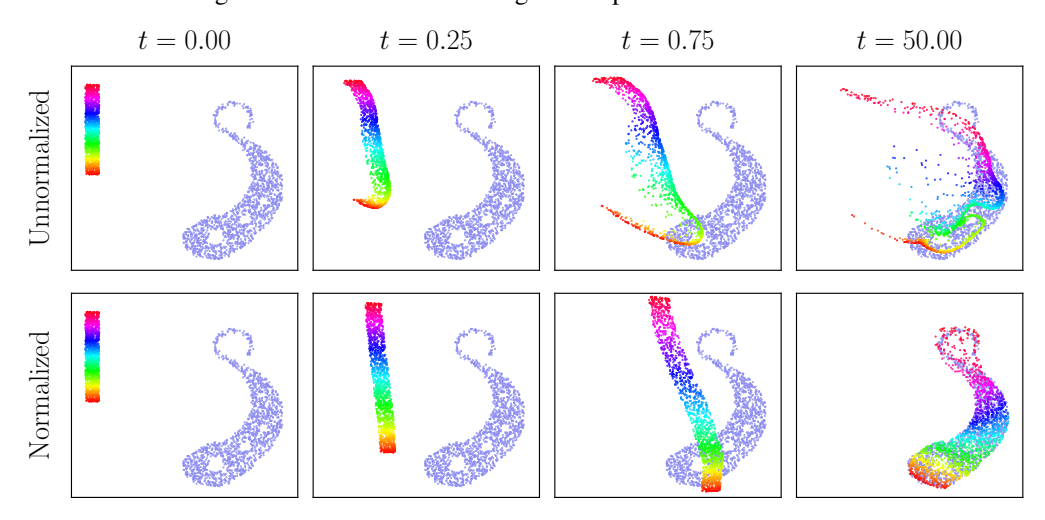


Figure 15: Gradient flow using unnormalized and normalized Gaussian kernels with $\sigma = 0.07$.

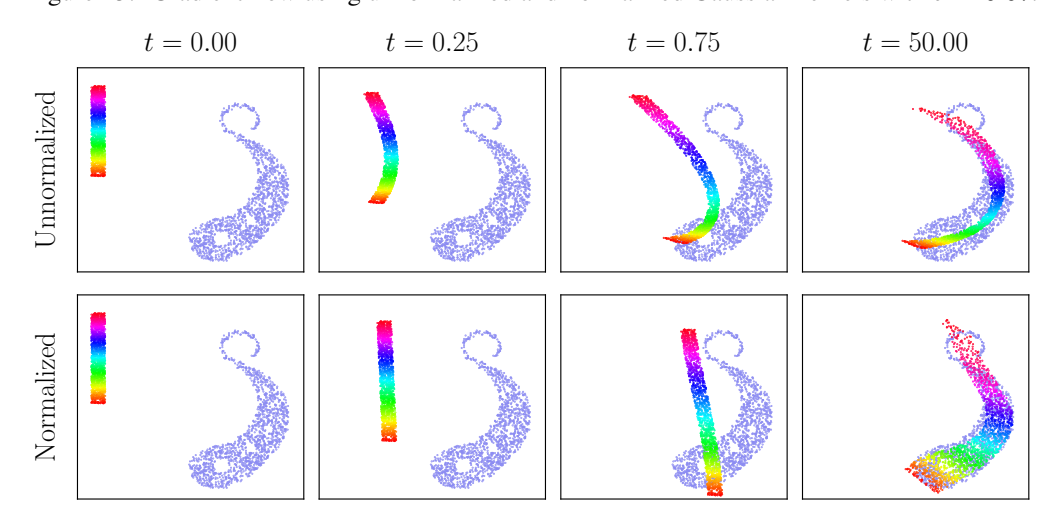


Figure 16: Gradient flow using unnormalized and normalized Gaussian kernels with $\sigma = 0.2$.

denotes the set of vertices of the source mesh in 3D, we define the standard Hamiltonian H(q, p) on (position, momentum) pairs $\mathbb{R}^{N\times 3}\times \mathbb{R}^{N\times 3}$ with:

$$H(q,p) = \frac{1}{2} \operatorname{trace}(p^{\top} K_q p) = \frac{1}{2} \sum_{i,j=1}^{N} (K_q)_{ij} \cdot p_i^{\top} p_j$$
, (51)

where $(K_q)_{ij} = \exp(-\|q_i - q_j\|^2/2\sigma^2)$ is a Gaussian kernel matrix. Starting from a source position $q(t=0) = (x_1, \dots, x_N)$, geodesic shape trajectories are parametrized by an initial momentum p(t=0) and flow along the coupled geodesic equation in phase space:

$$\dot{q}(t) = +\frac{\partial H}{\partial p}(q(t), p(t)), \qquad \dot{p}(t) = -\frac{\partial H}{\partial q}(q(t), p(t))$$
 (52)

that we integrate to time t=1 using an explicit Euler scheme with a step size $\delta t=0.1$. The partial derivatives of the Hamiltonian are computed automatically with PyTorch.

Shape Interpolation. In Figure 5a from the main manuscript, we display the source position $q(t=0)=(x_1,\ldots,x_N)$ in red and a target configuration in blue. In Figure 5b, we use the L-BFGS algorithm to optimize with respect to the initial shooting momentum p(t=0) the mean squared error between the position of the geodesic q(t=1) at time t=1 and the target configuration. Then, we use Eq. (52) to sample the geodesic curve q(t) at time t=-0.5, t=0.5 and t=1.5.

In Figure 5c, we use the exact same implementation but normalize the Gaussian kernel matrix K_q into a diffusion operator Q_q before defining a "normalized" Hamiltonian H(q,p):

$$H(q, p) = \frac{1}{2} \operatorname{trace}(p^{\top} Q_q p) . \tag{53}$$

For the sake of simplicity, we do not use the mesh connectivity information and rely instead on constant weights to define the mass matrix M. Although our Hamiltonian is now defined via the iterative Sinkhorn algorithm, automatic differentiation lets us perform geodesic shooting without problems. Finally, in Figure 5d, we identify every Gaussian component $\mathcal{N}(x_i, \Sigma_i)$ with a cloud of 6 points sampled at $(x_i \pm s_{i,1}e_{i,1}, x_i \pm s_{i,2}e_{i,2}, x_i \pm s_{i,3}e_{i,3})$, where $e_{i,1}$, $e_{i,2}$ and $e_{i,3}$ denote the eigenvectors of Σ_i with eigenvalues $s_{i,1}^2$, $s_{i,2}^2$ and $s_{i,3}^2$. This allows us to use the same underlying point cloud implementation.

I DETAILS ON POINT FEATURES LEARNING

Q-DiffNet. DiffusionNet (Sharp et al., 2022) is a powerful baseline for learning pointwise features on meshes and point clouds. It relies on two main components: a diffusion block and a gradient feature block. The diffusion block approximates heat diffusion spectrally rather than solving a sparse linear system. In Q-DiffNet, we replace this truncated spectral diffusion with our normalized diffusion operator, using a Gaussian convolution as the original smoothing operator. Given a shape \mathcal{S} with vertices $X \in \mathbb{R}^{N \times 3}$, features $f \in \mathbb{R}^{N \times P}$ and a diagonal mass matrix M, we define:

Q-Diff
$$(f, X, M; \sigma) = Q(X, M, \sigma)^m f$$
 where $Q(X, M, \sigma) = \Lambda_{\sigma} K_{\sigma}(X, X) M \Lambda_{\sigma}$. (54)

In the above equation, K_{σ} is a Gaussian kernel of standard deviation σ , Λ_{σ} is the diagonal scaling matrix computed from Algorithm 1, and m is the number of application of the operator. The scaling Λ_{σ} is recomputed in real time at each forward pass using 10 iteration of Algorithm 1, without backpropagation. Repeating the operator m times allows for simulating longer diffusion times. In practice, we use m=2.

Like DiffusionNet (Sharp et al., 2022), Q-DiffNet supports multi-scale diffusion: the layer takes input features of shape $B \times C \times N \times P$ and applies separate diffusion per channel, using learnable scales $(\sigma_c)_{c=1}^C$. In DiffusionNet, typical values are C=256, P=1. For speed efficiency, we use C=32, P=8 in our experiments, which preserves the total amount of features in the network.

Architecture Integration. We integrate Q-DiffNet into the ULRSSM pipeline (Cao et al., 2023), which is designed for unsupervised 3D shape correspondence. This framework trains a single network \mathcal{N}_{Θ} , usually DiffusionNet (Sharp et al., 2022), that outputs pointwise features for any input shape \mathcal{S} . Inputs to the network typically consist of spectral descriptors such as WKS (Aubry et al., 2011) or HKS (Sun et al., 2009) – among these, WKS is generally preferred. Raw 3D coordinates (xyz) are also used in some settings.

 Point Cloud Inputs. Although DiffusionNet (Sharp et al., 2022) can operate on point clouds since it does not require mesh connectivity, it still depends on (approximate) Laplacian eigenvectors (Sharp & Crane, 2020). When working with point clouds, spectral descriptors like WKS (Aubry et al., 2011) change because they rely on the underlying Laplacian eigendecomposition. To isolate the effect of our proposed Q-operator, we minimize variability across experiments and use WKS descriptors (Aubry et al., 2011) computed from the mesh-based Laplacian for all experiments, even when retraining DiffusionNet (Sharp et al., 2022) or ULRSSM (Cao et al., 2023) on point clouds. This ensures consistent inputs across surface and point-based variants.

Loss Functions. The ULRSSM pipeline uses Laplacian eigenvectors during training to compute functional maps C_{12} and C_{21} from the predicted pointwise features f_1 and f_2 (Donati et al., 2020; Sharp et al., 2022; Cao et al., 2023). These maps are fed in the original ULRSSM losses: orthogonality, bijectivity, and alignment (Cao et al., 2023). For consistency, we retain these losses unchanged. Mesh-based models use ground-truth mesh eigenvectors, point cloud versions use approximate point cloud eigenvectors. Our Q-DiffNet model uses mesh eigenvectors, while the Q-DiffNet (Q-FM) variant uses eigenvectors derived from our normalized diffusion operator.

Dataset. We train on the standard aggregation of the remeshed FAUST (Bogo et al., 2014; Ren et al., 2019) and SCAPE datasets (Anguelov et al., 2005), using only intra-dataset pairs within the training split. We follow the standard train/test splits used in prior baselines (Donati et al., 2020; Sharp et al., 2022; Cao et al., 2023). The 44 shapes from the remeshed SHREC dataset (Melzi et al., 2019) are reserved exclusively for evaluation.

Training. We use the exact ULRSSM setup (Cao et al., 2023), where we train the network for 5 epochs with a batch size of 1, using Adam optimizer with an initial learning rate of 10^{-3} and cosine annealing down to 10^{-4} . Training takes 6h on a single V100 GPU.